

D^2 SLAM: Decentralized and Distributed Collaborative Visual-inertial SLAM System for Aerial Swarm

Hao Xu, Peize Liu, Xinyi Chen, Shaojie Shen

Abstract—In recent years, aerial swarm technology has developed rapidly. In order to accomplish a fully autonomous aerial swarm, a key technology is decentralized and distributed collaborative SLAM (CSLAM) for aerial swarms, which estimates the relative pose and the consistent global trajectories. In this paper, we propose D^2 SLAM: a decentralized and distributed (D^2) collaborative SLAM algorithm. This algorithm has high local accuracy and global consistency, and the distributed architecture allows it to scale up. D^2 SLAM covers swarm state estimation in two scenarios: near-field state estimation for high real-time accuracy at close range and far-field state estimation for globally consistent trajectories estimation at the long-range between UAVs. Distributed optimization algorithms are adopted as the backend to achieve the D^2 goal. D^2 SLAM is robust to transient loss of communication, network delays, and other factors. Thanks to the flexible architecture, D^2 SLAM has the potential of applying in various scenarios.

Index Terms—Swarms, aerial systems: perception and autonomy, multi-robot systems, sensor fusion

I. INTRODUCTION

LOCATION technology is critical for highly autonomous robot swarm. Unlike mono mobile robots, swarm robotics need to estimate not only the state of each robot itself but also the state of the other robots. In recent years, simultaneous localization and mapping technology [1]–[4] for swarm robot, including aerial swarm has been greatly developed, these method are well-known as cooperative SLAM (CSLAM) or multi-robot SLAM.

Due to the size, weight, and power (SWaP) constrain of the aerial robot platform, the primary goal of most SLAM algorithms on aerial robots is to provide input for navigation (planning and control). Let's explore a few categories of practical tasks of aerial swarm to find the technology requirements of CSLAM. First category is self-assemble aerial swarm [5] and cooperative transportation [6] using of multiple UAVs, in this case, UAVs in the swarm require very precise relative localization (centimeter level) to cooperative with each other in very near distance (usually lower than a meter). Second category is inter-UAV collision avoidance [7] and formation flight [8], in this case, high accuracy relative localization (centimeter-level to decimeter-level) at few meters are required to avoid collision and maintain flight formation. Another typical task of aerial swarm is cooperative exploration of

All authors are with the Department of Electronic and Computer Engineering, Hong Kong University of Science and Technology, Hong Kong, China. {hxubc, pliuan, xchencq}@connect.ust.hk, eeshaojie@ust.hk (Corresponding author: Hao Xu.)



Fig. 1: Indoor aerial swarm formation flight with 5 UAVs [10]. The customized UAV platforms are circled in the snapshot.

unknown space. Based on our experience [9], we found it's essential to have a high accuracy relative localization when UAVs are near to each other to avoid inter-drone collision for this task. However, when UAVs start to explore the unknown space and fly far away from each other, the relative localization accuracy is not important, and the global consistency of the estimate trajectories is more important to built up the global map of the unknown space.

As a summary, at close distances, aerial swarm need high precision relative localization, while for longer distances, high precision relative positioning is not necessary (and difficult to achieve) and global consistency of state estimation is more important. Beyond the relative localization, among all these task, the high accuracy ego-motion estimation is essential for maintain stable flight.

In addition to the requirements given by the tasks, the CSLAM algorithms are also limited by the communication conditions. The common modes of mutual communication of robot swarm include centralized communication (for example, using a Wireless Local Area Networks) and communication using wireless ad hoc networks. The former is commonly found in laboratory environments. However, in real-world environments, robot swarm, especially aerial swarm with high mobility, need to work in a variety of complex environments where simple centralized communication is difficult to guarantee. A more practical approach is to use wireless ad hoc networks [1], where neighboring robots form a mesh

network, which communication ability is limited by occlusion, communication distance, interference, etc. These networks have better communication conditions when UAVs are close to each other, but have limited communication bandwidth and stability at longer distances.

Moreover, computation architecture of CSLAM may be different. Broadly speaking, there are two major architectures of SLAM technology for robot swarms, centralized and decentralized. Centralized CSLAM computes information on a ground-station server, which makes it dependent on a stable network connection, while decentralized CSLAM is suitable for a wider range of situations. A well-designed decentralized approach does not depend on a stable network homology. Compared to decentralized (but redundant) CSLAM approaches, e.g. [1], distributed CSLAM has advantages of a reduced (but not costless) computation overhead per aircraft, and better privacy performance: only partial information needs to be broadcast [4]. The biggest advantage of distributed SLAM is that it opens up the possibility of scaling CSLAM to large-scale swarm.

Based on the realistic requirements and communication conditions as well as the SWaP limitations of autonomous UAVs, we propose a novel CSLAM system, D^2 SLAM, a decentralized and distributed visual-inertial SLAM system. D^2 SLAM is designed as a highly flexible sparse SLAM system. The state estimation of D^2 SLAM is a combination of two parts, *near-field state estimation* and *far-field state estimation* for aerial swarm. Here we have borrowed the terms from electromagnetism. In this paper, near-field state estimation is defined as estimating high precision real-time local state (ego-motion estimation, e.g., VIO) and high precision real-time relative state between UAVs when UAVs' onboard sensor has field-of-view (FoV) overlap (near-field-of-view), UAVs are with good communication (near for wireless communication). Far-field state estimation is defined as estimating trajectories with global consistency when UAVs are far from each other or in non-line-of-sight (far-field-of-view), UAVs have only limited communication (far for wireless communication). We believe that the combination of these two state estimations covers well the state estimation problems we summarized above that aerial swarm need to face.

The module to achieve near-field estimation in D^2 SLAM is named as D^2 VINS (decentralized and distributed visual-inertial navigation system). D^2 VINS is designed as a cooperative VIO system for multi-robot using sparse features. Similar to typical single-robot VIO systems (e.g., VINS-Mono [11]), D^2 VINS maintain local map with sliding window, and graph-based optimization is adopted for state estimation.

Due to the general limitation of visual SLAM, one concern is that we can only get the highly accurate real-time relative state with D^2 VINS if the sensor's FoV has overlapped in a short period, even when UAVs are very close to each other, i.e., the near-field-of-view constraint. Fortunately, the omnidirectional vision system has been shown to be exceptionally effective for aerial swarm to solve the FoV issue in our previous work [1]. In this paper, we also employ an improved omnidirectional visual frontend to overcome the near-field-of-view constraint.

When D^2 VINS works with an omnidirectional vision front end, the near-field-of-view is relaxed, i.e., D^2 VINS will not be limited by the UAV's yaw angle, it can be performed as long as UAVs are in line-of-sight, with common features in environments and good communication. Nevertheless, the commercial stereo camera, e.g., Intel Realsense D435i, has been widely adopted by the state-of-the-art aerial swarm [9], [12], so they are also supported by D^2 SLAM. Another advantage of a stereo camera system over a quad camera system is that it requires lower computational power and is suitable for UAVs with limited computing resources. However, when using these cameras, it is necessary to carefully set the yaw of the UAV to get the best relative state estimation accuracy, but this is out of the scope of this paper.

The core of far-field estimation is D^2 PGO (decentralized and distributed pose graph optimization). D^2 PGO is designed to provide global consistent state estimation, providing relative localization and global localization information even when the UAV is far away from each other or out of line of sight using pose graph optimization. Unlike D^2 VINS, D^2 PGO is designed to work even when the communication condition is poor, so we designed an asynchronous distributed pose graph optimization algorithm based on ARock.

Our near and far field estimation is not independent from each other, D^2 VINS and multi-UAV loop closure detection module together provide relative measurements (loop-edge) to D^2 PGO, while D^2 PGO provides initialization information to D^2 VINS when the two UAVs meet. The process from far to near can also be understood as a coarse-to-fine localization process.

Finally, although the core of D^2 SLAM is the state estimation with the sparse SLAM, it can be easily extended to dense mapping, and we have experimentally demonstrated the effects of dense mapping using D^2 PGO in combination with RGB-D cameras or depth generation.

The main contributions of this paper are as follows:

- We propose a novel decentralized and distributed SLAM system and tested it on aerial swarm platform in real-world experiment. Specifically, D^2 SLAM is capable of estimating high-accuracy ego-motion state and also high-accuracy relative state when UAV are close to each other while estimate trajectories with global consistency when UAV are far from each other or in non-line-of-sight.
- We propose an distributed visual inertial state estimator based on ADMM-based for multi-robot.
- We propose an ARock-based multi-robot asynchronous distributed pose graph optimization algorithm.
- The proposed D^2 SLAM is tested on aerial swarm platform in real-world experiment. The code and our custom datasets will be open-sourced.

II. RELATED WORKS

A. Distributed Bundle Adjustment

Recently, distributed bundle adjustment problems have been developed in the structure from motion (SfM) community [13], [14]. A Eriksson et. al. proposed a distributed bundle adjustment approach by using a consensus-based distributed

optimization framework [13]. This method splits a large number of camera pose into several disjoint sets and uses proximal splitting methods to build a distributed optimization solution form (also equivalent to Alternating Direction Method of Multipliers (ADMM) method), which requires exchanging the information of all feature points in each iteration during the optimization process. The disadvantage of the [13] method is that the landmark information has to be exchanged among agents at each iteration of the optimization, which induces a huge communication overhead for the SFM problem. An improvement of this approach was proposed by Zhang et al. [14], in which they used a *camera consensus* approach, splitting landmarks into disjoint sets to build distributed optimization problems. In each iteration of the distributed optimization, only the camera pose information needs to be exchanged, and this approach is shown to have better convergence performance and much smaller communication bandwidth usage compared to [13].

In D^2 VINS, we follow the idea of [14] and divide the feature points into disjoint sets to build the ADMM problem thus solving the collaborative VIO problem in a distributed manner.

B. Distributed Pose Graph Optimization

PGO [15], [16], derived from the factor graph [17], is one of the key techniques for simultaneous localization and mapping (SLAM), and is generally used for re-localization [11], [18] and dense mapping [19]. When researchers turned their attention to multi-robot collaboration, the PGO approach was naturally introduced in CSLAM as well [20]–[22]. Early attempts at PGO in CSLAM were accomplished by solving the pose graph problem using a centralized server [22]. However, centralized PGO suffers from scalability and communication issues in swarm robot systems. The first distributed SLAM approach, DDF-SAM, was proposed by Cunningham et al. [20]. It uses a constrained factor graph, as does its improved version DDF-SAM2 [21]. However, both methods keep a neighborhood graph on each agent and optimize it on each agent, which wastes computational resources and lacks scalability.

Real progress on DPGO started with the Distributed Gauss-Seidel (DGS) approach proposed by Choudhary et al. [4]. In this method, the PGO problem is first transformed into a linear problem and then solved in a distributed manner using the Gauss-Seidel method [23]. Later, the ASAPP method, based on distributed gradient descent, was proposed by Tian et al. [24]. It can be seen as a distributed and asynchronous version of Riemann gradient descent [25]. The highlight of that work is that it was the first to take communication into account and deliver an asynchronous DPGO approach. The subsequent work of Tian et al. [26] introduces the DC2-PGO method using the Distributed Riemann-Staircase method, which is a certifiably correct DPGO method. The above DPGO methods are currently used in several practical SLAM systems, including DOOR-SLAM [3], which utilizes DGS, and Kimera-multi [2], which uses DC2-PGO.

III. SYSTEM OVERVIEW

First of all, this paper continues the symbol system of our previous paper [1], which is not repeated here. In this paper, we assume the aerial swarm contains of N UAVs, and each UAV has a unique ID $i \in \{1, 2, \dots, N\}$. If not specifically stated, these UAVs pick the initial position of the drone k to establish the global reference system of the swarm. See Sect. III-G for details on how to establish the reference system uniformly among the UAVs.

A. State Estimation Problem of CSLAM on aerial swarm

State estimation is the core of CSLAM. The objectives of the CSLAM for aerial swarm is: For an aerial swarm that contains a maximum of n homogeneous drones, the state estimation problem can be represented as follows. For every drone $k \in \mathcal{D}$, estimate the 6-DOF pose ${}^{v_k}\mathbf{T}_i^t$ for every drone $i \in \mathcal{D}_a^k$ at time t in drone k 's local frame. The state estimation problem for drone k can be split into two parts:

- 1) Estimating the ego-motion state of drone k in a local frame, i.e., $\hat{\mathbf{T}}_k^t$.
- 2) Estimating the state of any other arbitrary drone i , i.e., ${}^{v_k}\hat{\mathbf{T}}_i^t$.

B. Global Consistency of the SLAM

In SLAM research [27], [28], global consistency of state estimation represents that the estimate results are drift-free, e.g., the ${}^{v_k}\hat{\mathbf{P}}_i^t$ do not drift along with the robot move. The opposite concept of global consistency is odometry [11], [29]: in SLAM, odometry usually refers to estimating a slightly drifting but locally accurate 3D (x, y, yaw) or 6D pose and an accurate velocity. We consider a state estimation algorithm based on onboard sensors, such as cameras, Lidars, IMU, as a SLAM algorithm when it has global consistency. Otherwise, it is considered odometry.

C. Decentralized vs Distributed

Although decentralized and distributed are often conflated, we argue that their meanings differ. Decentralized emphasize that algorithms running on multiple nodes have no central node presence, but decentralized algorithms has chance to have a large amount of redundant computation. Distributed algorithms emphasize that computation (or other resources, such as storage) is distributed across multiple nodes and non-redundant computation but may still have a central node presence.

The final goal of this thesis is to propose a distributed and decentralized (D^2) CSLAM algorithm, D^2 SLAM. We believe this is a suitable algorithmic architecture for autonomous aerial swarms. It can effectively avoid failures caused by the loss of a single node, is more robust to communication loss, and ensures that the swarm has sufficient autonomy to split into multiple sub-swarms or form a new large swarm. At the same time, it can make better use of the computational resources carried by each drone.

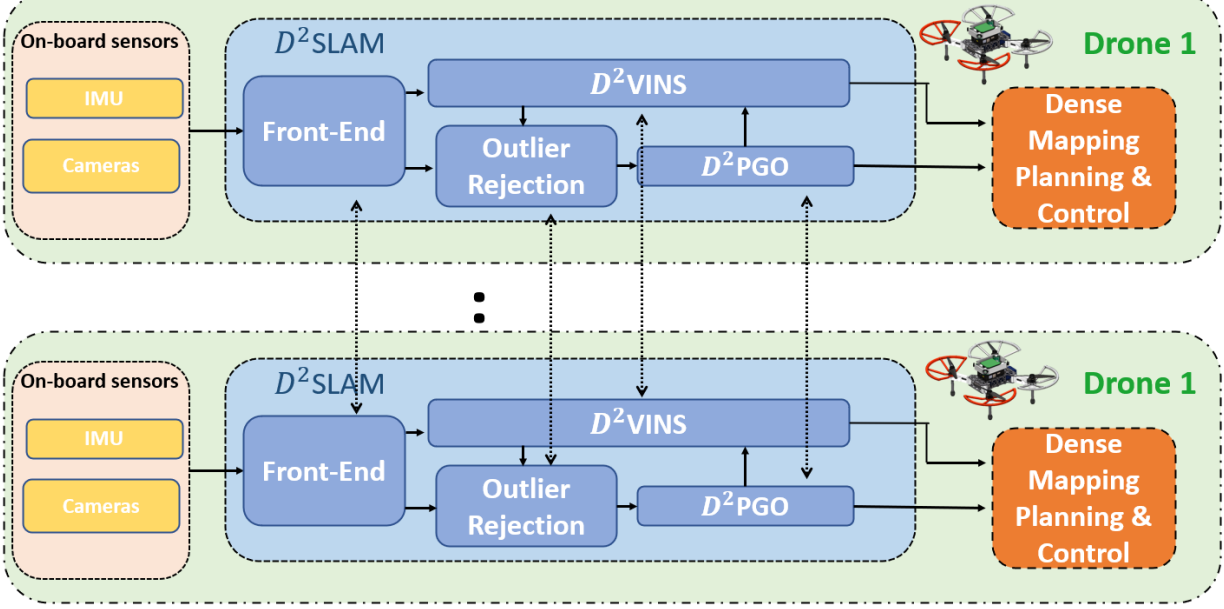


Fig. 2: The architecture of D^2 SLAM. The D^2 SLAM is independently running on each UAV. The data will be first processed by front-end and then sent to back-end for state estimation. Results will be utilized for dense mapping, planning and control.

D. Operating Conditions of D^2 SLAM

D^2 SLAM is designed as a very flexible SLAM system. Specifically, it degrades to independent stand-alone SLAM or VIO when it receives environment limitations or communication restrictions. It is proved that aerial swarm still guarantee stable flight and even perform formation flight for a short period with only standalone VIO [8]. In the following, we will discuss these limitations in detail.

Firstly, communication is essential for cooperative SLAM, UAV collaboration without communication is not covered in this thesis. If communication is unavailable, D^2 SLAM will degenerate into a single-robot SLAM system.

When communication exists, the operating of D^2 SLAM depends on the specific communication conditions. Near-field state estimation requires a larger amount of data exchange and real-time performance, so a good and low-latency network environment is needed. Far-field state estimation requires less latency and communication.

Secondly, like all visual sparse SLAM systems, in some environments, such as grass or rough walls, D^2 SLAM can still perform the ego-motion estimation. However, it is challenging to use these features to match between keyframes for relative localization and loop closure detection, i.e., D^2 SLAM degrades to VIO. In other environments, such as cluttered indoor and outdoor environments, D^2 SLAM can use environmental features for matching and thus complete state estimation.

Thirdly, D^2 SLAM is designed to perform near-field estimation when there is FoV overlap between UAVs in a short period and there are enough common features. When using FoV limited cameras, this requires the yaw angle of the UAVs to be aligned. As previously stated, D^2 SLAM accepts omnidirectional vision as input, so yaw angle no longer limits the near-field state estimation in this case. Nevertheless, near-

field state estimation still requires that the UAV is in line of sight for a short period. However, thanks to the local accuracy of D^2 SLAM, the loss of a few tens of seconds of common feature does not bring significant loss of relative state estimation. We argue that near-field state estimation is no longer necessary for swarm control & planning when the UAV is not in the line of sight for a long period or is too far away that no valid common features are available.

E. Communication Modes

In order to let D^2 SLAM work in various situations, we designed two communication modes for him: **compact** and **greedy**. In the compact mode, we minimize the communication overhead, using measures such as sending compact descriptors, performing distributed loop closure detection (Sect. IV-E) and only sending information for near-field state estimation at a near distance (Sect. IV-D). In greedy mode, each drone shares all its information as much as possible, which is suitable for the case of good network conditions but causes communication overhead. D^2 VINS can operate independently to D^2 PGO in this mode.

F. D^2 SLAM System Architecture

The architecture of D^2 SLAM is shown in Fig. 2. As previously stated, D^2 SLAM is a decentralized and distributed SLAM system, which means that the frontend and state estimation are performed on each UAV independently. For D^2 SLAM on each UAV, the visual input is first processed by the front-end for key frame extraction, sparse feature tracking, and loop closure detection, and these results are sent to the back-end for D^2 VINS and PGO outlier rejection. D^2 VINS and D^2 PGO are used for near-field state estimation and far-field state estimation. Finally, the estimated result is sent to dense map building, planning, and control.

G. Multi-robot Map Merging

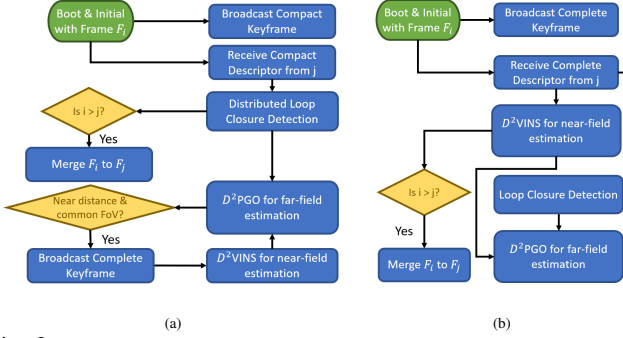


Fig. 3: Flow charts of multi-robot state initialized and map merging. a) Map-merging procedure in compact mode, saving more communication; b) Map-merging in greedy mode, suitable for scenarios where communication bandwidth is not constrained.

One of the key concerns of CSLAM is the selection of reference systems between different robots, and there are usually two designs: 1) each robot maintains its own reference system and transforms the estimated reference system between different robots [1]; 2) all robots share the same reference system [3], [30], [31], for which has a more concise mathematical representation than the first design but also brings the problem of initialization and fusion of the reference system. D^2 SLAM adopts the second method. Unlike some studies [30], [31] that use the ground-truth pose to initialize the robot pose in a global frame which reduces the system's flexibility, we allow the reference system and sparse map of different robots to be fused at runtime in D^2 SLAM for better system flexibility.

Each robot establishes a local reference frame \mathbf{F}_i with the start position as the origin at boot time, where i is the ID of the drone. As this drone meets other robots or travels across the same place visited by another drone j , this drone will generate relative measurements to another drone, so we perform inter-drone map merging based on the relative measurements. D^2 SLAM on both drones selects the smaller reference frame id of the encountered UAV as the new reference system. We convert the sliding window, prior (Sect. V-C) in D^2 VINS and the keyframe pose (Sect. VI) in D^2 PGO of the larger id UAV to the new reference system based on their relative measurements.

The map merging procedure under compact communication mode is shown in Fig. 3a. In this flow, we use distributed loop closure detection (Sect. IV-E) and broadcast complete keyframe information only when the drone is close for near field state estimation (Sect. IV-D). Furthermore, in the case of greedy communication, D^2 VINS will skip D^2 PGO to map-merging directly, as shown in Fig. 3b.

It is worth noting that once the map merge is done, subsequent state estimation will no longer require the above process.

IV. FRONT-END

D^2 SLAM provides a flexible and efficient front-end for visual inputs, the front-end accepts multiple type of camera configuration, including omnidirectional camera, stereo pin-hole camera and even RGB-D camera. As shown in the Fig.

4, our front-end consists of several parts: 1) pre-processing the fisheye image for omnidirectional camera setup; 2) general pre-processing to extract feature points and global descriptors; 3) feature tracking on local drone; 4) multi-drone real-time frame matching; 5) distributed loop closure detection.

A. Fisheye images preprocessing

In this paper, we use a quad fisheye camera system, as shown in the Fig. 6. Compared to the dual fisheye camera system [1], [32], it uses the cameras' FoV more effectively and generates higher quality depths. Due to these advantages, this configuration is also adopted in SLAM research [33] and some advance product in UAV industry (e.g. DJI Mavic 3).

The fisheye camera captures images with a significant distortion, which makes it difficult to apply existing vision techniques directly, a example of the raw fisheye images is shown in the Fig. 5a. Inspired by [34], we first reproject these images into cylindrical projection, as shown in Fig. 5b, and then perform subsequent processing. As proved by [34], directly apply of CNNs trained using public datasets on these reprojected images deliver good results.

B. General pre-processing

We use MobileNetVLAD [35] to build a global descriptor for each camera view. We use SuperPoint [36] to extract feature points, PCA is also adopted for reduce the dimension of the feature descriptors. These techniques have been verified in our previous work [1], we do not elaborate here.

C. Sparse Feature Tracking

Currently, two types of sparse feature tracking are applied to sparse visual SLAM: 1, using the Lucas-Kanade (LK) method (VINS-Mono [11]); 2, using descriptors for matching (ORB-SLAM [37]). The LK-based approach is more robust when the environmental features are sparse (e.g., grass), but it cannot handle large parallax. Furthermore, using this method for large parallax multi-view feature matching is challenging, which is essential for multi-drone feature matching and performing relative pose extraction after loop closure detection. The descriptor-based approaches, especially CNN-based approaches, can handle large parallax and efficiently perform multi-drone matching or loop closure detection, but it does not work well in places with sparse environmental features.

In this paper, multi-drone feature matching and robustness are both critical. So we use a hybrid front-end to balance these requirements, as shown in Fig. 5b. The maximum number of feature points tracked by each camera view is N_{max} (100-150 in practice). On each camera view, we first extract $N_{max_{sp}}$ (50-100) sparse features and their descriptors using SuperPoint [36], assuming that the number of successful extractions is N_{sp} . We choose the SuperPoint feature because it is more robust than the ORB feature employed in [37]. The inter-frame tracking of these feature points is done using a kNN matcher with ratio test [38]. We then use Shi-Tomasi corner detector to extract $N_{max} - N_{sp}$ feature points and track them with LK method. Only SuperPoint features are used for loop closure

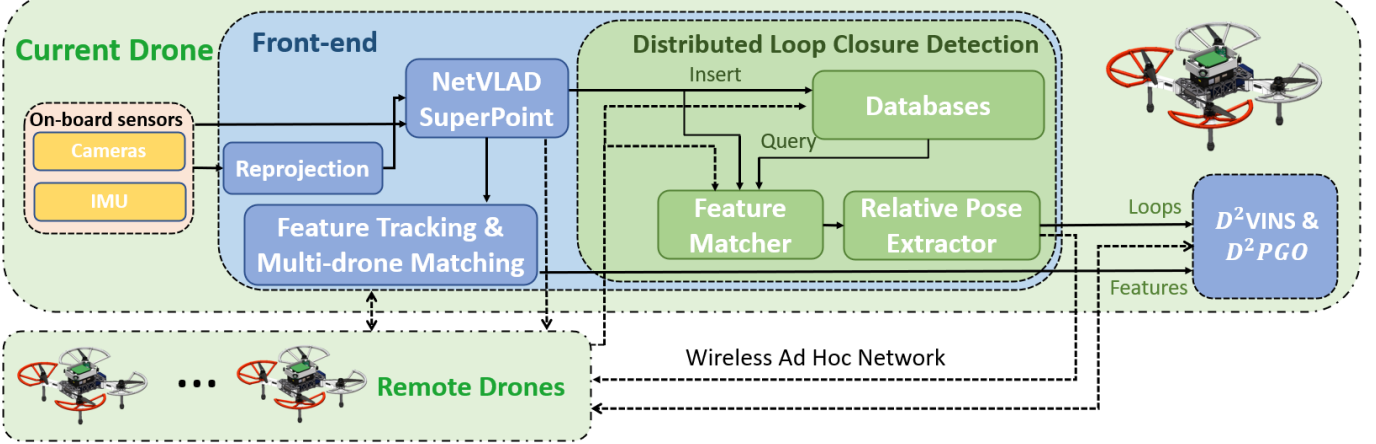


Fig. 4: The front-end of D^2 SLAM. The visual data is first processed by reprojection, next send to extract global descriptor and features, then send to feature tracking, multi-drone feature matching and loop closure detection. The final results will be fused in the back-end.

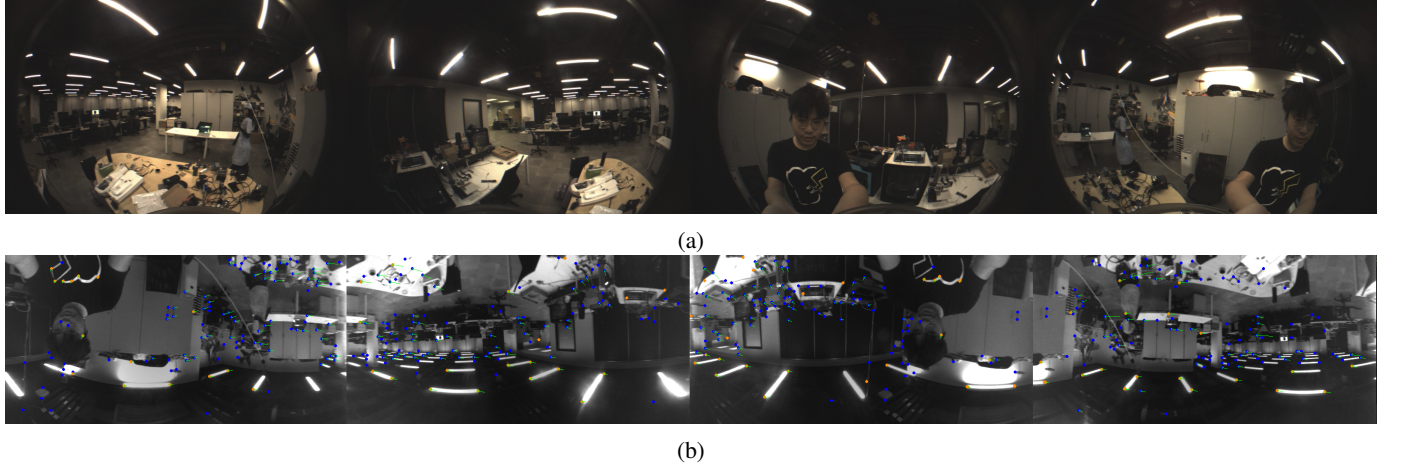


Fig. 5: A demonstration of fisheye images: (a) raw fisheye images (b) reprojected fisheye images and feature tracking. The blue points are SuperPoint features and the orange points are LK features. The green arrows are the inter-frame movements of these features.

detection and multi-drone matching. That is, LK feature points only contribute to the ego-motion estimation. Once feature tracking is complete, we determine whether a new frame is a keyframe based on the parallax and the number of new feature points.

Another thing worth noting is the multi-view feature tracking between different cameras on same UAV. It is easy to handle when using stereo input: We directly match the SuperPoint feature point and LK optical flow for the left and right cameras. For quad fisheye cameras, each fisheye camera will only have feature points in common with the neighboring camera's half-plane, as shown in Fig. 6. So we only perform feature matching on SuperPoint features in the corresponding half-planes and pre-panning the positions of these feature points according to the camera's internal and external parameters as initialization values when solving for LK optical flow.

D. Multi-drone Sparse Feature Matching

When a keyframe arrives, we first search the sliding window for the most recent keyframe that matches it. Two keyframes are considered to match when their global descriptors have

a inner product greater than a threshold τ_{mg} (default is 0.8). If the search is successful, we perform kNN feature matching with ratio test on the Superpoint features of these two keyframes to establish the correspondence between the features. The successfully matched features are considered to belong to the same landmark and sent to the backend for near-field state estimation.

In compact communication mode, to save communication bandwidth, we only broadcast the complete keyframe information, including SuperPoint features and the global descriptors of each camera view, to other drones in the swarm when the following conditions are met:

- existing other UAVs are predicted to be in close range based on the existing state estimation results (within 5 m in an indoor environment),
- the nearby drones have efficient FoV overlap with current drone if drones are using non-omnidirectional camera configuration.

One issue here is how the relative states of the aerial swarm are initialized, which will be detailed later in Sect. III-G

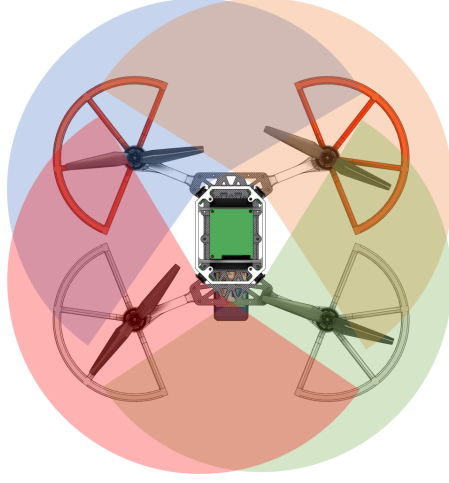


Fig. 6: A demonstration of the configuration of quad fisheye cameras. The transparent areas are the FoV of each camera.

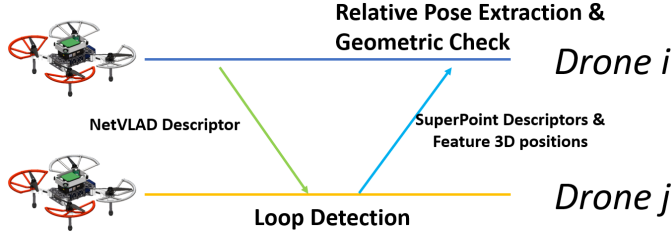


Fig. 7: A demonstration of distributed loop closure detection.

E. Distributed Loop Closure Detection

In loop closure detection, we use Faiss [39] to build the whole image descriptor database with the MobileNetVLAD descriptor as index. Nevertheless, a distributed loop closure detection architecture have been widely used in recently multi-robot SLAM approaches [2], [3], which has been shown to reduce the required communication bandwidth. In D^2 SLAM, the distributed loop closure detection for inter-drone loop closure detection is also adopted, as shown in Fig. 7. When drone i receiving a keyframe from remote drone k , we first perform whole image searching by Faiss. Next, we return the matched keyframe to drone i and perform feature matching with kNN method and relative pose extraction by using Perspective-n-Point (PnP). Finally, we use geometrics check and consistency check for outlier rejection and the final loop edge is sent to backend for pose graph optimization.

The noteworthy thing is that D^2 SLAM can use quad fisheye cameras as input. In this case, single-camera Perspective-n-Point (PnP) [40] for relative pose extraction and geometry verification, which the commonly used in loop closure detection [1]–[3], [11], does not apply. Instead, we need to solve a multi-camera PnP problem. Specifically, we use the UPnP RANSAC algorithm [41], a multi-camera PnP method, for pose estimation initial and outlier rejection and then use the inlier result to solve a bundle adjustment problem for multi-camera PnP to obtain a more accurate pose. The UPnP RANSAC and the follow bundle adjustment refine in our implementation is from OpenGV [42].

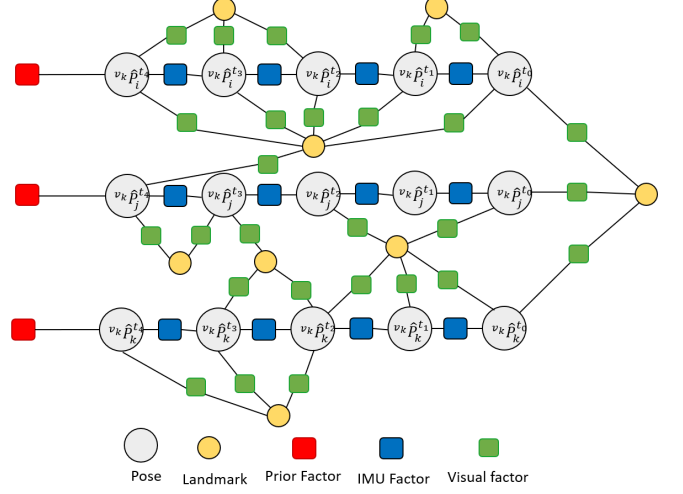


Fig. 8: A demonstration of the factor graph of D^2 VINS.

V. NEAR-FIELD STATE ESTIMATION: D^2 VINS

A. Problem formulation

In order to conduct near-field state estimator for D^2 SLAM, we propose D^2 VINS, a cooperative visual-inertial-odometer estimator. D^2 VINS is designed to real-time estimate accurate 6-DoF odometry of self drone and nearby drones which satisfies the previous stated conditions. D^2 VINS uses a graph optimization framework with sliding window. The state estimation problem for D^2 VINS can be represented using a factor graph [17], as shown in Fig. 8. We estimate the states in the sliding window by solving the maximum a posteriori (MAP) inference of this factor graph using the distributed non-linear-least-square optimization. The state of the collaborative visual-inertial-odometry problem is defined as

$$\mathcal{X} = \left[\begin{array}{c} v_k \tilde{\mathbf{T}}_0^{t_0}, v_k \tilde{\mathbf{T}}_0^{t_1}, \dots, v_k \tilde{\mathbf{T}}_0^{t_{m-1}}, \mathbf{b}_0^{t_0}, \mathbf{b}_0^{t_1}, \dots, \mathbf{b}_0^{t_{m-1}}, \\ \dots, v_k \tilde{\mathbf{T}}_1^{t_0}, v_k \tilde{\mathbf{T}}_1^{t_1}, \dots, v_k \tilde{\mathbf{T}}_1^{t_{m-1}}, \mathbf{b}_1^{t_0}, \mathbf{b}_1^{t_1}, \dots, \mathbf{b}_1^{t_{m-1}}, \\ l_0, l_1, l_2, \dots, l_L \end{array} \right]^T, \quad (1)$$

where $v_k \tilde{\mathbf{T}}_i^{t_j}$ is the estimated pose of UAV i at time t_j in the local frame of UAV k , m is the length of the sliding window and n is the number of the drones in the swarm, $\mathbf{b}_i^{t_j} = [v_k \mathbf{v}_i^{t_j}, b_a^{t_j}, b_g^{t_j}]$ is the velocity, acceleration bias and angular velocity bias of the IMU of UAV i at time t_j , l_j is the state of landmark p and L is the total number of the landmarks. In this paper, we use the inverse depth parametrization [43] for landmarks, i.e. l is the inverse depth from the keyframe that landmark l_j attached to and the landmark l_j . For convenience, we denote the set of all poses in \mathcal{X} as \mathcal{T} . The optimization problem for collaborative visual-

inertial-odometry is formulated as,

$$\begin{aligned} \min_{\mathcal{X}} \left\{ \|\mathbf{r}_p - \mathbf{H}_p \mathcal{X}\|^2 + \sum_{k \in \mathcal{B}} \left\| r_{\mathcal{B}}(\tilde{z}_{b_k}^{b_{k+1}}, \mathcal{X}) \right\|_{\Sigma_{\mathcal{B}}} + \right. \\ \left. \sum_{k \in \mathcal{L}} \rho(\|r_{\mathcal{L}}(\tilde{z}_{l_k}, \mathcal{X})\|_{\Sigma_{\mathcal{L}}}) \right\}, \quad (2) \\ \text{s.t. } \mathbf{P}_i \in \mathbf{SE}(3), \forall \mathbf{P}_i \in \mathcal{T} \end{aligned}$$

where $\rho(\cdot)$ is the Huber norm [44], $\|\cdot\|_{\Sigma}$ is the Mahalanobis norm, \mathcal{B} is the set of IMU factors, $\mathbf{r}_{\mathcal{B}}$ is the residual of the IMU measurement factor, \mathcal{L} is the set of visual measurements, and $\mathbf{r}_{\mathcal{L}}$ is the visual measurement residual, $\mathbf{r}_{\mathcal{B}}$ and $\mathbf{r}_{\mathcal{L}}$ are define in [11] and well known to the community; $\|\mathbf{r}_p - \mathbf{H}_p \mathcal{X}\|^2$ is the prior factor generated from previous marginalization, which will be detailed in Sect. V-C.

B. Distributed Optimization of Collaborative visual-inertial-odometry problem

1) *ADMM method for decentralized and distributed optimization*: The target of decentralized and distributed optimization is to solve the problem,

$$\begin{aligned} \sum_{i=1}^n f_i(\mathbf{x}_i), \quad (3) \\ \text{s.t. } \mathbf{x}_i = \mathbf{z}, \end{aligned}$$

using decentralized (and distributed) ADMM method [14], [45], where \mathbf{x}_i is the local state for agent i and \mathbf{z} is the global state, the problem Eq. (4) can be solved by iteratively perform the following update on each agent i ,

$$\mathbf{x}_i^{t+1} = \text{argmin}_{\mathbf{x}_i} \left\{ f_i(\mathbf{x}_i) + \frac{\rho}{2} \|\mathbf{x}_i - (\mathbf{z}^t - \mathbf{u}^t)\|^2 \right\} \quad (4)$$

$$\mathbf{z}^{t+1} = \frac{1}{n} \sum_{i=1}^n \mathbf{x}_i^{t+1} \quad (5)$$

$$\mathbf{u}_i^{t+1} = \mathbf{u}_i^t + \mathbf{x}_i^{t+1} - \mathbf{z}^t, \quad (6)$$

e.g. each agent i solves the a new optimization problem Eq. (4) in each iteration and updates its estimate states optimization problem by averaging the results obtained by other agents.

2) *Distributed optimization for D^2 VINS*: Rewritten Eq. (2) to the form of decentralized optimization (3), we have,

$$\begin{aligned} \min_{\mathcal{X}_i} \sum_{i=1}^N f_{cvio_i}(\mathcal{X}_i) \\ f_{cvio_i}(\mathcal{X}_i) = \|\mathbf{r}_{p_i} - \mathbf{H}_{p_i} \mathcal{X}_i\|^2 + \sum_{k \in \mathcal{B}} \left\| r_{\mathcal{B}}(\tilde{z}_{b_k}^{b_{k+1}}, \mathcal{X}_i) \right\|_{\Sigma_{\mathcal{B}}} \\ + \sum_{k \in \mathcal{L}} \rho(\|r_{\mathcal{L}}(\tilde{z}_{l_k}, \mathcal{X}_i)\|_{\Sigma_{\mathcal{L}}}) \\ \text{s.t. } \mathcal{X}_i = \mathbf{E}_i \mathcal{X}, \\ \text{s.t. } \mathbf{P}_j \in \mathbf{SE}(3), \forall \mathbf{P}_j \in \mathcal{T}_i \quad (7) \end{aligned}$$

where \mathcal{X}_i is the local state on agent i , which will be detailed introduced in Sect. V-B3, \mathbf{E}_i project the global state \mathcal{X} to local state \mathcal{X}_i , $f_{cvio_i}(\mathcal{X}_i)$ is the subproblem of the global optimization problem Eq. (2) on agent i . Follow Eq. (4)-(6),

the iteration update of solving collaborative VIO problem (7) is,

$$\begin{aligned} \mathcal{X}_i^{t+1} = \arg \min_{\mathcal{X}_i} f_{cvio_i}(\mathcal{X}_i) + h(\mathcal{X}_i) \\ \text{s.t. } \mathbf{P}_i \in \mathbf{SE}(3), \forall \mathbf{P}_i \in \mathcal{T}_i \quad (8) \end{aligned}$$

$$h(\mathcal{X}_i) = \frac{1}{2} \sum_{\mathbf{P}_j \in \mathcal{T}_i} \left\| \log((\mathbf{P}_j^t)^{-1} \mathbf{P}_j^k) + \tilde{\mathbf{P}}_j^{k,t} \right\|_{\Sigma_{\rho_T}} \quad (9)$$

$$\begin{aligned} \tilde{\mathbf{P}}_j^{k,t+1} = \frac{1}{n_i} \sum_{j=1}^{n_i} (\mathbf{P}_j^k)^{t+1}, \forall \mathbf{P}_j \in \mathcal{T}_i \quad (10) \\ (\tilde{\mathbf{P}}_j^{k,t+1}) = (\tilde{\mathbf{P}}_j^{k,t}) + \log((\mathbf{P}_j^{t+1})^{-1} (\mathbf{P}_j^k)^t), \forall \mathbf{P}_j \in \mathcal{T}_i, \quad (11) \end{aligned}$$

where \mathcal{X}_i^t is the estimate local state of agent i in the t -th iteration, \mathcal{T}_i is the set of the poses in \mathcal{X}_i , \mathbf{P}_j the j -th pose in \mathcal{T}_i , \mathcal{L}_i is the set of the landmarks partitioned to drone i for solving, \mathcal{B}_i is the set of the IMU factors of drone i , the detailed of the \mathcal{X}_i^{t+1} , \mathcal{T}_i and \mathcal{L}_i will be introduced later in Sect. V-B3, $\log(\cdot)$ is the logarithm map of the Lie group $\mathbf{SE}(3)$ [46], which will be detailed in Sec. V-B4, $h(\mathcal{X}_i)$ is the consensus item to ensure the local state \mathcal{X}_i is consistent with the global state \mathcal{X} , inside $h(\mathcal{X}_i)$, the first item $\sum_{P \in \mathcal{T}_i} \left\| \log((P_i^t)^{-1} P_i^k) + \tilde{P}_i^{k,t} \right\|_{\Sigma_{\rho_T}}$ is to ensure the poses are consistent among drones and the second item $\rho_{\mathcal{L}} \sum_{l_i \in \mathcal{L}_i} \|l_i - l_i^t\|$ is to ensure the convergence of the distributed optimization as proved in [14]. The full algorithm of the distributed optimization for collaborative VIO is shown in Algorithm 1.

Algorithm 1: Distributed optimization for Collaborative VIO on drone i

Input: n drones, m landmarks, iter iterations, ρ and ρ_T .
Output: n drones' local states \mathcal{X}_i .
1 Initialize \mathcal{X}_i and \mathcal{X} , \mathcal{T}_i , \mathcal{L}_i .
2 **for** $t = 1$ to iter **do**
3 Solve the local optimization problem (8) with \mathcal{X}_i
4 Broadcast the poses \mathcal{T}_i in local state \mathcal{X}_i to all
 drones
5 Update \mathcal{X}_i with by averaging poses among swarm
 with Eq. (10).
6 Update the states for auxaliry variables $\{\tilde{\mathbf{P}}_j^k\}$
 using Eq. (11).

3) *Problem Splitting*: As we discussed in Sect. II-A, a key concern in optimization with ADMM is how the problem and state are partitioned. In D^2 VINS, we divide the landmarks \mathcal{L} into disjoint sets $\{\mathcal{L}_0, \mathcal{L}_1, \dots, \mathcal{L}_N\}$ and use this to partition the problem and state, where the set of the landmarks partitioned to drone i is denoted as \mathcal{L}_i . For every landmark l_k in \mathcal{L} , l_k is partitioned to \mathcal{L}_i if drone i first discovered l_k . And we define the set of all poses that are in \mathcal{X} and have measurements to the landmark in \mathcal{L}_i is \mathcal{T}_i , and \mathcal{X}_i is define as,

$$\mathcal{X}_i = \left[\mathcal{T}_i, \mathcal{L}_i, \mathbf{b}_i^{t_0}, \mathbf{b}_i^{t_1} \dots \mathbf{b}_i^{t_{m-1}} \right]^T, \quad (12)$$

where $\mathbf{b}_i^{t_0}, \mathbf{b}_i^{t_1} \dots \mathbf{b}_i^{t_{m-1}k}$ are the state of the velocity and IMU bias of drone i , they are only essential for local optimization. Due to the presence of the hybrid tracking feature method (Sect. IV-C), \mathcal{X}_i necessarily contains all i 's pose in \mathcal{X} . This ensures that once all remote aircraft are disconnected, D^2 VINS can still estimate the ego-motion, i.e., degrade to a single-robot VIO.

4) *Optimization on Manifold*: One key problem in SLAM is the optimization on the manifold. In Alg. 1, Problem (8) is solved by Riemannian trust region (RTR) method [25] to ensure the pose state is on $\mathbf{SE}(3)$ group, i.e., $\mathbf{P}_i \in \mathbf{SE}(3), \forall \mathbf{P}_i \in \mathcal{T}_i$. In addition, the auxiliary states $\{\hat{\mathbf{P}}_j^k\dots\}$ are defined on $\mathbf{se}(3)$. We use the logarithm map [46] to transform the error $(\mathbf{P}_j^{t+1})^{-1}(\mathbf{P}_j^k)^t$ defined on $\mathbf{SE}(3)$ into $\mathbf{se}(3)$. Another problem is that Eq. (10) needs to average the rotations, which we solve using the quaternion averaging algorithm [47] well known in the aerospace field.

5) *Convergence Analysis*: Due to the complexity of the problem, existing graph-based VIO researchers [11], [48], [49] rarely mention the convergence of optimization methods. Instead, these VIO algorithms emphasize the use of good initialization to guarantee the convergence of the algorithm. Therefore, we also discuss only the convergence of the Alg. 1 in the case of good initialization, which well be shown in Appendix A.

6) *Implementation*: In this paper, Problem (8) is solved using Ceres-solver [50] with Dogleg strategy [51] with dense Schur solver as the linear solver. In this implementation, we use Local Parameterization from ceres to add the on manifold constraints of the poses, it's combination with the dog leg strategy can be consider as an instance of the RTR method [25].

Another thing worth noting is that, due to 10, Alg. 1 is a synchronous method, which requires the UAV to wait for the results of other UAVs at each iteration. The synchronization method may cause a decrease in efficiency when the communication environment is poor. Fortunately, we have found in practice that relaxing the condition of 10, i.e., averaging the state of the other drones received most recently each time without waiting, also yields results close to those of the synchronous method. We refer to this method as asynchronous D^2 VINS. A comparison of asynchronous versus synchronous D^2 VINS will be shown in VIII-A.

C. Sliding Window & Marginalization

D^2 VINS uses a sliding window to manage keyframes, and each drone manages only its keyframes. Similar to [11], when a new frame is added, the previous latest frame in is discarded if it is not a keyframe, otherwise, the oldest keyframe is discarded. After the sliding window is updated, D^2 VINS will push the latest sliding window information to the other drone in the swarm.

When the old keyframes are discarded, we linearize each subproblem ($f_{cvio_i}(\mathcal{X}_i)$) of the problem (7) and compute a new set of priors $\{(\mathbf{r}_{p_0}, \mathbf{H}_{p_0}), (\mathbf{r}_{p_1}, \mathbf{H}_{p_1}) \dots (\mathbf{r}_{p_{N-1}}, \mathbf{H}_{p_{N-1}})\}$ using the Schur complement by dropping the old states. This procedure is well-known as marginalization [11], [48]. In

marginalization, these subproblems are treated as independent, so the marginalization process is also run distributively. Nevertheless, the problem (7) is solved with states averaged over different drones (Eq. 10), so the marginalization among drones are consistent, i.e., on different drones, the states are linearized with the same or very close linearization points.

D. Initialization

The initialization of D^2 VINS is divided into two parts, the initialization of the local keyframe and the initialization of the remote drone. D^2 VINS uses stereo or multi-camera, we directly use triangulation to initialize the location of landmarks has measurements with enough baseline (0.05cm in practical) from multi-cameras or from motion, and also use IMU prediction to initialize the subsequent keyframe pose from local drone. After initialization, we add priors to the unobservable part (x, y, z, yaw) of the first frame to increase stability. For the case of multiple drones, we use PnP RANSAC (or gPnP) to initialize the pose of the remote keyframe when the coordinate system reference of the remote drone is different from the local drone. The migration and merging of different reference systems will be detailed in Sect. III-G

VI. FAR-FIELD STATE ESTIMATION: D^2 PGO

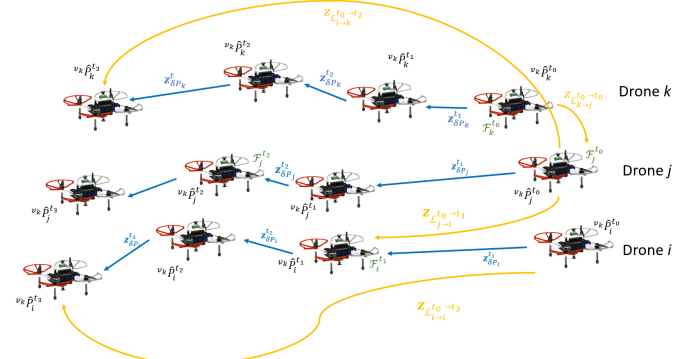


Fig. 9: The pose graph for D^2 PGO.

Complete far-field estimation includes the estimation of global consistent trajectories (D^2 PGO) and real-time global consistent odometries. We use pose graph for modeling the trajectories estimation problem: keyframes of the trajectory are represented as nodes on the graph, and different keyframes are connected by edges representing relative poses, as shown in Fig. 9. The pose graph can be expressed as a factor graph, and assuming that the measurement is Gaussian distributed, thus is the well-known pose graph optimization problem [17]:

D^2 PGO uses two-stage optimization to decentralize and distribute the solution of the pose graph optimization problem for multiple drones.

$$\begin{aligned} \min_{\mathbf{x}_i} \sum_{(i_{t_0}, j_{t_1}) \in \mathcal{E}} & \left\| v_k \hat{\mathbf{P}}_j^{t_1} - v_k \hat{\mathbf{P}}_i^{t_0} - v_k \hat{\mathbf{R}}_i^{t_0} \mathbf{z}_{\mathbf{P}_i \rightarrow j}^{t_0 \rightarrow t_1} \right\|_{\Sigma_t}^2 \\ & + \left\| v_k \hat{\mathbf{R}}_j^{t_1} - v_k \hat{\mathbf{R}}_i^{t_0} \mathbf{z}_{\mathbf{R}_i \rightarrow j}^{t_0 \rightarrow t_1} \right\|_{\Sigma_R}^2, \\ \text{s.t. } & v_k \hat{\mathbf{R}}_i^{t_0} \in SO(3), \end{aligned} \quad (13)$$

where \mathcal{E} is the set of all edge, including loop closure edge (generated by D^2 VINS and loop closure detection) and ego-motion edge (generated by D^2 VINS), ${}^{v_k}\mathbf{R}_i^t$ is the rotation part of ${}^{v_k}\hat{\mathbf{T}}_i^t$, and ${}^{v_k}\mathbf{p}_i^t$ is the translation part of ${}^{v_k}\hat{\mathbf{T}}_i^t$, \mathbf{x} is the full state of the pose graph:

$$\mathcal{X} = \left[{}^{v_k}\hat{\mathbf{T}}_0^{t_0}, {}^{v_k}\hat{\mathbf{T}}_0^{t_1}, \dots {}^{v_k}\hat{\mathbf{T}}_0^{t_{M-1}}, \dots {}^{v_k}\hat{\mathbf{T}}_1^{t_0}, \right. \\ \left. {}^{v_k}\hat{\mathbf{T}}_1^{t_1}, \dots {}^{v_k}\hat{\mathbf{T}}_{N-1}^{t_{M-1}} \right], \quad (14)$$

where N is the number of drones, M is the number of keyframes of each drone.

D^2 PGO uses two-stage approach to solve the pose graph optimization problem (13) decentralize and distributedly. Rewriting the pose graph optimization problem (13) in distributed manner (4), we have:

$$\min_{\mathbf{x}_i} \sum_{i=0}^{N-1} f_{pgo_i}(\mathbf{x}_i) \\ f_{pgo_i}(\mathbf{x}_i) = \sum_{(i_{t_0}, j_{t_1}) \in \mathcal{E}^i} \left\| {}^{v_k}\hat{\mathbf{p}}_j^{t_1} - {}^{v_k}\hat{\mathbf{p}}_i^{t_0} - {}^{v_k}\hat{\mathbf{R}}_i^{t_0} \mathbf{z}_{\mathbf{p}_i \rightarrow j}^{t_0 \rightarrow t_1} \right\|_{\Sigma_R}^2 \\ + \left\| {}^{v_k}\hat{\mathbf{R}}_j^{t_1} - {}^{v_k}\hat{\mathbf{R}}_i^{t_0} \mathbf{z}_{\mathbf{R}_i \rightarrow j}^{t_0 \rightarrow t_1} \right\|_{\Sigma_R}^2, \\ \text{s.t. } {}^{v_k}\hat{\mathbf{R}}_i^t = \mathbf{E}_{i_t}^R \mathbf{z}, {}^{v_k}\hat{\mathbf{p}}_i^t = \mathbf{E}_{i_t}^p \mathbf{z}, {}^{v_k}\hat{\mathbf{R}}_i^t \in SO(3), \quad (15)$$

where x_i is the state of the drone i , \mathcal{E}^i is the set of edges of the drone i .

In the first stage of D^2 PGO, we use the initialize the rotation of the pose graph to avoid local minima. In the second stage, we refine the optimization of the pose graph. In addition to pose graph optimization, we also adopt a outlier rejection module to reject outliers in the pose graph optimization problem (13).

Finally, we combine the pose graph optimization result with the VIO result to obtain the global consistent trajectory of each drone:

$${}^{v_k}\hat{\mathbf{T}}_i^{t_1} = {}^{v_k}\hat{\mathbf{T}}_i^t (\tilde{\mathbf{T}}_i^t)^{-1} \tilde{\mathbf{T}}_i^{t_1}, \quad (16)$$

where ${}^{v_k}\hat{\mathbf{T}}_i^t$ is the pose of the latest keyframe of UAV i in D^2 PGO and $\tilde{\mathbf{T}}_i^t$ is the odometry estimation with D^2 VINS of this keyframe, $\tilde{\mathbf{T}}_i^{t_1}$ is the real-time odometry estimation with D^2 VINS.

A. ARock for Distributed Optimization

We use ARock [52], an asynchronous distribution optimization algorithm to solve the PGO. ARock uses follow iteration update to solve the distributed optimization problem (3), the [52]:

$$\hat{\mathbf{x}}_i^t = \arg \min_{\mathbf{x}_i} f_i(\mathbf{x}_i) + \mathbf{x}_i \sum_{r \in \mathcal{R}(i)} z_{ri,r}^t + \frac{\gamma}{2} |\mathcal{R}(i)| \cdot \|\mathbf{x}_i\|^2 \quad (17)$$

$$z_{ri,i}^{t+1} = z_{ri,i}^t - \eta_k ((z_{ri,i}^t + z_{ri,r})/2 + \gamma \hat{\mathbf{x}}_i^t) \quad \forall r \in \mathcal{R}(i), \quad (18)$$

where $\mathcal{R}(i)$ is the set of neighbors of agent i , $(\cdot)^t$ means state of t -th iteration, η_k and γ are two parameters. $z_{ij,i}, z_{ij,j}$ are the dual variables for agent i and its neighbor j , and will be update by agent i and j respectively. We rewriting

Algorithm 2: ARock for distributed optimization

Input: n drones, m landmarks, $iter$ iterations.

1 Initialize $y_{ij,i}^0, y_{ij,j}^0$ for all i, j to 0.
2 **for** $t = 1$ to $iter$ **do**
3 Solve the local optimization problem (19)
4 Update the dual states $y_{ir,i}^t$ with Eq. (20).
5 Broadcast the dual state $y_{ir,i}^t$ to all drones
6 **if** Convergence **then**
7 Break

the update rule replacing the dual variables $z_{ri,i}^t, z_{ri,r}^t$ with $y_{ij,i} = -z_{ij,i}/\gamma, y_{ij,j} = -z_{ij,j}/\gamma$,

$$\hat{\mathbf{x}}_i^t = \arg \min_{\mathbf{x}_i} f_i(\mathbf{x}_i) + \sum_{r \in \mathcal{R}(i)} \frac{\gamma}{2} \|\mathbf{x}_i - y_{ri,r}^t\|^2 \quad (19)$$

$$y_{ir,i}^{t+1} = y_{ir,i}^t - \eta_k ((y_{ir,i}^t + y_{ir,r})/2 - \hat{\mathbf{x}}_i^t) \quad \forall r \in \mathcal{R}(i) \quad (20)$$

Alg. 2 shows the full algorithm of ARock for decentralized optimization. Unlike the Alg. 1 we used earlier, ARock is an asynchronous algorithm. We only need to use the latest received dual variables from remote without running the equations synchronously, as in Eq. (19)-(20), which means that ARock is more insensitive to communication delays. Moreover, Alg. 2 is proved to be linear convergence [52].

B. Asynchronous Distributed Rotation Initialization

The nonlinearities in the pose graph problem come from rotations. When rotations are properly initialized, the pose graph optimization problem approaches a linear least square problem and is easily solved. The rotation initialization technique has been proved effective in avoiding local minima of the pose graph optimization [53]. The target of rotation initialization is find the solution or a approximate solution for the rotation part of problem (13), which is also known as the rotation averaging problem [54]:

$$\min_{\mathbf{x}_i} \sum_{(i_{t_0}, j_{t_1}) \in \mathcal{E}^i} \left\| {}^{v_k}\hat{\mathbf{R}}_j^{t_1} - {}^{v_k}\hat{\mathbf{R}}_i^{t_0} \mathbf{z}_{\mathbf{R}_i \rightarrow j}^{t_0 \rightarrow t_1} \right\|_{\Sigma_R}^2 \\ \text{s.t. } {}^{v_k}\hat{\mathbf{R}}_i^t \in SO(3). \quad (21)$$

An efficient and powerful algorithm for solving this problem is Chordal relaxation [55]. In this algorithm, we first solve the problem by relaxing the $SO(3)$ constrain of (21):

$$\min_{\mathbf{x}_i} \sum_{(i_{t_0}, j_{t_1}) \in \mathcal{E}} \left\| {}^{v_k}\bar{\mathbf{R}}_j^{t_1} - {}^{v_k}\bar{\mathbf{R}}_i^{t_0} \mathbf{z}_{\mathbf{R}_i \rightarrow j}^{t_0 \rightarrow t_1} \right\|_{\Sigma_R}^2 \\ + \sum_{\bar{\mathbf{R}}_i^t \in \mathcal{R}_i} \| {}^{v_k}(\bar{\mathbf{R}}_i^t)_3 - \mathbf{v}_i \|_{\Sigma_g}^2, \quad (22)$$

where \mathcal{R}_i is the set of all rotations in \mathbf{x}_i , $\bar{\mathbf{R}}_i^t$ is a 3×3 matrix of drone i at time t , $\| {}^{v_k}(\bar{\mathbf{R}}_i^t)_3 - \mathbf{v}_i \|$ is the vertical prior, this item is added because the roll pitch angle of VIO is observable and thus can be used as a prior to enhance the initialization [53], ${}^{v_k}(\bar{\mathbf{R}}_i^t)_3$ is the third row of matrix $\bar{\mathbf{R}}_i^t$, $\mathbf{v}_i = (\bar{\mathbf{R}}_i^t)^T \mathbf{g}$, $\mathbf{g} = [0, 0, 1]^T$, $\tilde{\mathbf{R}}_i^t$ is the odometry output rotation of drone i

Algorithm 3: Asynchronous Distributed Rotation Initialization for drone i

Input: n drones, ϵ for termination, max_iter iterations, min_iter to avoid early exiting.

- 1 Initialize $y_{ij,i}^0, y_{ij,j}^0$ for all i, j to 0.
- 2 **for** $t = 1$ to max_iter **do**
- 3 Solve the local optimization problem (19) with f_i defined from (25)
- 4 Update the dual states $y_{ir,i}^t$ with Eq. (20).
- 5 Broadcast the dual state $y_{ir,i}^t$ to all drones
- 6 **if** $\frac{1}{|\mathcal{R}_i|} \sum_{\bar{R} \in \mathcal{R}_i} \|(\bar{\mathbf{R}})^t - (\bar{\mathbf{R}})^{t-1}\|_F / \|(\bar{\mathbf{R}})^t\|_F < \epsilon$ **and** $iter > min_iter$ **then**
- 7 **break**
- 8 **for** $\bar{R} \in \mathcal{R}_i$ **do**
- 9 Recover the rotation ${}^{v_k} \hat{\mathbf{R}}_i^t$ with Eq. (24)

at time t . Problem (22) is a linear least square problem which can be efficiently solved by a linear solver. Then, we can recover the rotation matrix by

$$\begin{aligned} {}^{v_k} \hat{\mathbf{R}}_i^t &= \operatorname{argmin}_{\hat{\mathbf{R}}} \| \hat{\mathbf{R}} - {}^{v_k} \bar{\mathbf{R}}_i^t \|_F^2, \\ \text{s.t. } \hat{\mathbf{R}} &\in \mathbf{SO}(3) \end{aligned} \quad (23)$$

where $\|\cdot\|_F$ is the Frobenius norm. Problem (23) has a closed form solution with SVD decomposition [54]:

$${}^{v_k} \check{\mathbf{R}}_i^t = \mathbf{S} \operatorname{diag}([1, 1, \det(\mathbf{S} \mathbf{V}^T)]) \mathbf{V}^T, \quad (24)$$

where ${}^{v_k} \check{\mathbf{R}}_i^t \in SO(3)$ is the initial result of ${}^{v_k} \hat{\mathbf{R}}_i^t$, $\mathbf{S} \mathbf{V}^T$ is the SVD decomposition of $\bar{\mathbf{R}}_i^t$.

In D^2 PGO, problem (22) is solved in a distributed manner, rewriting the problem as,

$$\begin{aligned} \min_{\mathbf{x}_i} \sum_{i=0}^{N-1} \left\{ \sum_{(i_{t_0}, j_{t_1}) \in \mathcal{E}_i} \left\| {}^{v_k} \bar{\mathbf{R}}_j^{t_1} - {}^{v_k} \bar{\mathbf{R}}_i^{t_0} \mathbf{z}_{\mathbf{R}_{i \rightarrow j}}^{t_0 \rightarrow t_1} \right\|_{\Sigma_R}^2 \right. \\ \left. + \sum_{\bar{\mathbf{R}}_i^t \in \mathbf{x}_i} \| {}^{v_k} (\bar{\mathbf{R}}_i^t)_3 - \mathbf{v}_i \|_{\Sigma_g} \right\}, \end{aligned} \quad (25)$$

Applying Alg. 2 to solve for problem (25) leads to the proposed asynchronous distributed rotation initialization algorithm, as shown in Alg. 3. The local optimization problem (bring (25) into (19)) in Alg. 3 is a linear least square problem, which is solved efficiently by using Cholesky factorization [56]. We terminate the iterations when the change in the state being optimized is small, as shown in Alg. 25 line 6, where $(\bar{\mathbf{R}})^t$ is the state after t iteration. Moreover, to prevent premature termination, e.g., no data was received at the beginning, we also set a minimum number of iterations.

C. Asynchronous Distributed Pose Graph Optimization

After completing the initialization, we build the perturbation problem of (15) with the initialization rotation,

$$\begin{aligned} \min_{\mathbf{x}_i^*} \sum_{i=0}^{N-1} f_{pgo_i}(\mathbf{x}_i^*) \\ f_{pgo_i}^*(\mathbf{x}_i^*) = \sum_{(i_{t_0}, j_{t_1}) \in \mathcal{E}_i} \left\| {}^{v_k} \hat{\mathbf{p}}_j^{t_1} - {}^{v_k} \hat{\mathbf{p}}_i^{t_0} - \boxplus({}^{v_k} \check{\mathbf{R}}_i^{t_0}, {}^{v_k} \delta \theta_i^{t_0}) \mathbf{z}_{\mathbf{p}_{i \rightarrow j}}^{t_0 \rightarrow t_1} \right\|_{\Sigma_p}^2 + \\ \left\| \boxplus({}^{v_k} \check{\mathbf{R}}_j^{t_1}, {}^{v_k} \delta \theta_j^{t_1}) - \boxplus({}^{v_k} \check{\mathbf{R}}_i^{t_0}, {}^{v_k} \delta \theta_i^{t_0}) \mathbf{z}_{\mathbf{R}_{i \rightarrow j}}^{t_0 \rightarrow t_1} \right\|_{\Sigma_R}^2, \\ \text{s.t. } {}^{v_k} \delta \theta_i^{t_0} = \mathbf{E}_{i_t}^R \mathbf{z}^*, {}^{v_k} \hat{\mathbf{p}}_i^{t_0} = \mathbf{E}_{i_t}^p \mathbf{z}^*, \end{aligned} \quad (26)$$

where $({}^{v_k} \hat{\mathbf{p}}_i^{t_0}, {}^{v_k} \delta \theta_i^{t_0})$ is the perturbation state of ${}^{v_k} \mathbf{T}_i^{t_0}$, where ${}^{v_k} \hat{\mathbf{p}}_i^{t_0}$ is the position of ${}^{v_k} \mathbf{T}_i^{t_0}$ and ${}^{v_k} \delta \theta_i^{t_0} \in \mathfrak{so}3$ is the perturbation state of the rotation. \mathbf{x}_i^* is the perturbation state of \mathbf{x}^i , and \mathbf{z}^* is the global perturbation state, $\boxplus(\mathbf{R}, \delta \theta) = \mathbf{R} \operatorname{Exp}(\delta \theta_i^{t_0})$ retracts $\mathfrak{so}3$ vector to $\mathbf{SO}(3)$ at \mathbf{R} [25], where $\operatorname{Exp}(\cdot)$ maps $\mathfrak{so}3$ to $SO(3)$ [57]. Unlike Eq (10) in [4], which also uses a two-step PGO, (26) is a nonlinear problem that avoids the accuracy problems of [4] due to linearization.

We also apply Alg. 2 to solve (26), which ensures that our algorithm is asynchronous. In addition, taking $f_{pgo_i}^*(\mathbf{x}_i^*)$ into (19) results in a nonlinear least square problem, which can be solved with Levenberg-Marquardt algorithm [58]. Finally, we use the change in the cost of $f_{pgo_i}^*(\mathbf{x}_i^*)$ to determine if it converges, and like Alg. 3, a minimum number of iterations is used to prevent premature exits. After the convergence, we recover the global pose with

$${}^{v_k} \hat{\mathbf{T}}_i^{t v_k} = \begin{bmatrix} \boxplus({}^{v_k} \check{\mathbf{R}}_i^{t_0}, {}^{v_k} \delta \theta_i^{t_0}) & \hat{\mathbf{p}}_i^t \\ 0 & 1 \end{bmatrix} \quad (27)$$

This algorithm is similar to Alg. 3, so we will not elaborate.

D. Convergence

ARock is shown to have good convergence performance, and we believe it can converge to optimality on the first stage of a typical linear least squares problem. The results of rotation initialization prove to be effective in avoiding subsequent iterative optimization into the wrong local optimum [53], thus ensuring that D^2 PGO can reach or close to the global optimum.

E. Outlier Rejection

Pairwise consistent measurement set maximization (PCM) [1], [3], [59] and Graduated non-convexity (GNC) [60] are currently mainstream outlier rejection methods currently applied to multi-robot PGO. The advantage of PCM is that it is completely decoupled from the back-end optimization, but the disadvantage is that the performance is lower when the pose graph is huge; GNC is embedded in the back-end optimization, and the advantage is that it is more efficient, but GNC is a synchronous algorithm. In D^2 PGO, we use a distributed version of PCM as in [1], which can avoid some of the efficiency problems of PCM at large scales, and we believe that its performance is sufficient for PGO solutions that do not require real-time.

F. Implementation

The first stage ensures that D^2 PGO can still estimate the trajectories correctly in a highly noisy environment. In real-world experiments, we do not always need the first stage because the yaw measurement of VIO is fairly accurate.

We implemented D^2 PGO using C++, where we solve the linear least square of rotation initialization with Eigen [61]’s LLT algorithm. And we use the Levenberg-Marquardt algorithm from Ceres-solver [50] for the second stage.

VII. SYSTEM SETUP



Fig. 10: Our experiment aerial platform, which equips four fisheye cameras, an onboard computer, and an all-in-one flight controller.

Our experimental aerial swarm includes several customized aerial robot platforms, one of them is shown in Fig. 10. The platform is modified from a commercial 3.5-inch cinewhoop FPV drone and is equipped with four fisheye cameras that cover a 360-degree field of view in the horizontal direction. The onboard computer is NVIDIA Xaiver NX with strong GPU computing power. Furthermore, we use a lightweight all-in-one flight controller with four electronic speed control (ESC) integrated and customized PX4 [62] flight control firmware to reduce takeoff weight. This drone has a takeoff weight of about 623g when using a 22.8v 1550mah battery, and its maximum endurance is about 10min, which is sufficient as a testing platform.

Moreover, as mentioned above, we have implemented the D^2 SLAM using C++. For the CNNs covered in the previous section, we inferece them with Onnxruntime [63] and enabled TensorRt for acceleration. On the onboard computer, we use int8 mode to maximize the running speed. In addition, we develop TaichiSLAM¹, a GPU-accelerated mapping module, as the mapping backend for the dense mapping experiments later on. TaichiSLAM is written in the high-performance computing language taichi [64]. Various algorithms, including OctoMap [65], TSDF & ESDF [66], submap fusion [67] to generate global consistent map, Marching cubes for mesh generation

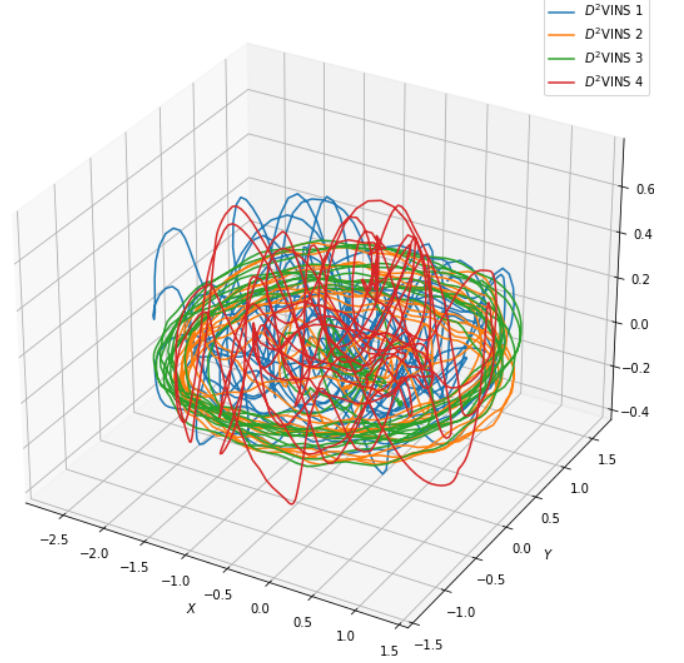


Fig. 11: The figure shows the estimated trajectories of D^2 VINS on TUM 4 dataset.

[68] and sparse topological skeleton graph generation [69], are implemented in TaichiSLAM. It should be noted that dense mapping algorithms are not the core part of D^2 SLAM, so we will not discuss them in detail.

VIII. EXPERIMENT

A. Evaluation of D^2 VINS

We first test D^2 VINS separately to verify the performance of our near-field state estimation. Here we use the greedy communication mode to allow D^2 VINS to operate independently. We test the stereo mode of D^2 VINS alone on public datasets TUM VI datasets [70] to verify our near-field state estimation capability on stereo cameras. Similar to [30], we align multiple data segments in the test to simulate a multi-drone scenario. In our tests, we do not use any ground truth to initialize D^2 SLAM, and all state estimation relies on the proposed method to run.

As shown in the Tab. I, our method demonstrates centimeter-level localization accuracy on the TUM VI dataset even though multiple robots on the tum dataset do not have sufficient common FoV most of the time. We demonstrate the effect of common FoV on D^2 VINS on the three robot evaluation. There is very accurate (2.5cm) relative localization between UAVs in the first 30s when common FoV is good, as shown in TUM 3 (30s), which is much better than the previous results in [10] and [1]. Throughout the full evaluation, the dataset still demonstrates centimeter-level relative localization accuracy, similar to the best localization accuracy we showed in the previous works, despite the absence of common FoV the vast majority of the time. This evaluation demonstrates that D^2 SLAM can perform highly accurate near-field state estimation even on stereo cameras, especially when the common field of view

¹<https://github.com/xuhao1/TaichiSLAM>

TABLE I: The table shows the statistical results of D^2 VINS compared to VINS-Mono [11] on TUM VI room dataset, where the ATE and RE are defined in [1]. TUM 3 is evaluate on TUM VI room {1, 2, 3}. TUM 3 has good common FoV at the first 30s, so we show the results individually. TUM 4 is evaluate on TUM VI room {1, 2, 3, 4}, and TUM 5 is {1, 2, 3, 4, 5}.

Dataset	Method	Avg. Traj. Len.	ATE _{pos}	ATE _{rot}	RE _{pos}	RE _{rot}
TUM 3 (30s)	D^2 VINS	18.3	0.030	0.99	0.025	0.77
	D^2 VINS (async)		0.035	1.63	0.025	0.74
	VINS-Mono		0.105	3.47	0.126	3.41
TUM 3	D^2 VINS	141.6	0.128	2.40	0.119	2.95
	D^2 VINS (async)		0.111	2.63	0.098	3.08
	VINS-Mono		0.176	2.84	0.216	3.81
TUM 4 (30s)	D^2 VINS	19.1	0.057	2.20	0.020	0.74
	D^2 VINS (async)		0.124	1.73	0.038	0.78
	VINS-Mono		0.108	4.01	0.113	2.76
TUM 4	D^2 VINS	100.9	0.115	2.44	0.080	1.72
	D^2 VINS (async)		0.105	2.18	0.082	1.85
	VINS-Mono		0.161	2.80	0.165	2.53
TUM 5 (30s)	D^2 VINS	19.2	0.079	1.35	0.039	0.73
	D^2 VINS (async)		0.108	4.50	0.037	0.89
	VINS-Mono		0.101	4.54	0.109	3.43
TUM 5	D^2 VINS	103.5	0.090	1.85	0.073	1.57
	D^2 VINS (async)		0.134	4.05	0.091	2.10
	VINS-Mono		0.176	3.03	0.176	2.80

TABLE II: The table shows the statistical results of D^2 VINS compared to VINS-Mono [11] on Omni datasets. Datasets from Omni 2 to Omni 5 corresponding to 2 to 5 UAVs. The average distance (Avg. Dis.) of the UAVs is also shown in the table.

Dataset	Avg. Traj. Len.	Avg. Dis.	Method	ATE _{pos}	ATE _{rot}	RE _{pos}	RE _{rot}
Omni 2	49.1	0.68	D^2 VINS	0.153	3.05	0.038	0.18
			VINS-Mono	0.237	6.60	0.271	0.52
Omni 3	48.2	0.7	D^2 VINS	0.168	2.26	0.045	0.43
			VINS-Mono	0.263	6.60	0.272	0.72
Omni 4	58.5	0.88	D^2 VINS	0.190	1.96	0.063	0.40
			VINS-Mono	0.262	4.94	0.317	0.75
Omni 5	45.4	1.03	D^2 VINS	0.167	3.72	0.073	0.52
			VINS-Mono	0.282	4.74	0.326	0.75

is sufficient. These results prove the value of D^2 SLAM for applications on widely used stereo camera UAV platforms. The estimated trajectories of D^2 VINS on TUM 4 dataset are shown in Fig. 11.

We further test D^2 VINS on custom omnidirectional camera datasets; the results are shown in the Tab. II. We collect the raw flight data using our custom UAV platform with a motion capture system as ground truth. Our method exhibits centimeter-level localization accuracy in all cases from 3 to 5 UAVs. We also note the fact that the relative localization accuracy slightly decreases as the relative distance between the UAVs increases. Fortunately, the need for inter-drone collision avoidance can still be met.

In comparison with VINS-Mono, we align VINS-Mono using the initial pose of ground truth to simulate the case of known UAV departure points as in [8]. Our results surpass all metrics compared to the state-of-the-art visual-inertial odometry algorithm, VINS-Mono. This proves the superiority of our algorithm over VINS-Mono in the multi-robot scenarios.

Furthermore, Tab. I shows the accuracy comparison of asynchronous D^2 VINS (D^2 VINS (async) in the table), we find that asynchronous D^2 VINS performs close to that of synchronous methods. However, in some cases, the accu-

racy of asynchronous methods can show some instability in ATE. Considering the advantages of asynchronous methods in communication, deploying asynchronous versions in realistic environments is an acceptable tradeoff.

B. Evaluation of D^2 SLAM

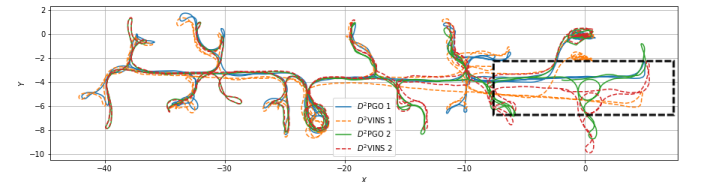


Fig. 12: The figure shows the estimated trajectories of D^2 SLAM on TUM Corr 2 Dataset. The TUM Corr 2 dataset is the combination of TUM VI corridor datasets {1, 2}. Two robots go through the same corridor sequentially in the black box section. The D^2 VINS trajectories show significant drift in the black box section, while the D^2 PGO trajectories have no significant drift, and the trajectories of the two robots are well aligned.

We test D^2 SLAM on the TUM VI corridor datasets to verify the performance of our far-field state estimation, where the real-time odometry and final pose graph estimated from

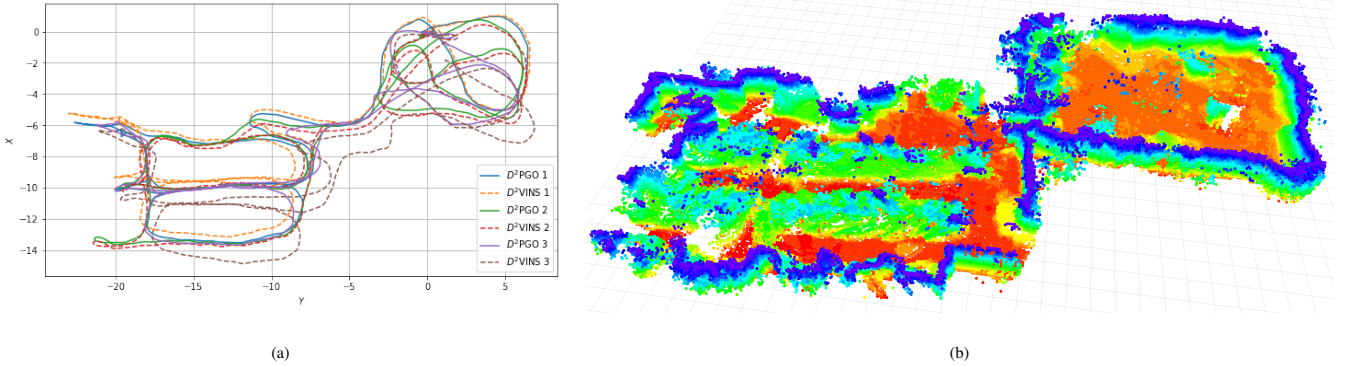


Fig. 13: The demonstration of D^2 SLAM on the HKUST RI dataset. a) The estimated trajectories of D^2 VINS and D^2 PGO of a three drone scenario. b) The dense map generated by D^2 SLAM using TSDF reconstruction, only the surface voxels from TSDF are shown.

the two-robot experiment is shown in Fig. 12. In this test, benefiting from the fact that the angle measurement of the VIO is fairly accurate, we only use the second stage of the D^2 PGO.

As shown in Fig. 12, unlike results from D^2 VINS drift away from the start point, trajectories estimated by D^2 PGO return to the starting point. In addition, D^2 PGO well align the trajectories of the two robots in the corridor (highlighted by the black box), while D^2 VINS results drift from each other because the two robots did not pass through the corridor simultaneously. This result exhibits that D^2 SLAM not only has good near-field accuracy and can demonstrate global consistency in the far-field case.

Fig. 13 shows the results of D^2 SLAM runs on our custom HKUST RI dataset. We collected this dataset using a drone equipped with a stereo depth camera, i.e. Intel RealSense D435i. We can see that D^2 VINS drifts away in Fig. 13a, but the estimated trajectory of D^2 PGO output maintains global consistency. Fig. 13b shows the results of TSDF reconstruction using D^2 PGO results, which are fused by using the submap fusion method implemented in TaichiSLAM. There are no evident drift in the map, which also verifies the global consistency of D^2 SLAM.

IX. CONCLUSION AND FUTURE WORK

In this chapter, we propose D^2 SLAM, a distributed and decentralized visual-inertial SLAM system. Our experiments verify that D^2 SLAM has real-time high-precision local localization capability and real-time high-precision relative localization when the UAVs are near each other, i.e., highly accurate near-field state estimation. Globally consistent trajectories can be estimated at the same time, i.e. global consistent far-field state estimation. We believe that D^2 SLAM's flexible sensor configuration, with state estimation capabilities suitable for various missions, including self-assembly aerial swarm, cooperative transportation, inter-drone collision avoidance, and unknown environments exploration, will contribute to the development of aerial swarm research.

The final D^2 SLAM presented in this thesis still has some limitations, which we will improve in the future: 1) Despite using a distributed backend, swarm scale growth is still

limited by communication capabilities, front-end computing capabilities. In the future, we will improve D^2 SLAM to make it apply to enormous aerial swarms. 2) Compared to our previous work, D^2 SLAM is designed as a more traditional visual SLAM work without introducing relative measurements, including UWB, visual recognition, etc. We believe that this allows D^2 SLAM to be adapted to more situations, such as occlusions that would cause inaccurate UWB measurements; and drones and ground robots that are difficult to identify accurately with visual detection. However, it is not difficult to add UWB or visual detection to D^2 SLAM, and we will explore the use of relative measurements in D^2 SLAM in the future.

Furthermore, we believe that D^2 SLAM can be applied not only to multi-robot systems but also as a distributed visual inertial SLAM system on a single robot, e.g., deploying several nodes running D^2 SLAM on a rigid UAV or ground robot for more accurate state estimation and robust in case of single node failure. Different nodes can even form distributed stereo cameras to measure the long-range environment. Alternatively, D^2 SLAM can be deployed on multi-rigid robots (e.g., multi-legged), and corresponding constraints can be introduced to help multi-rigid robots estimate their state and environment more accurately and provide redundancy.

APPENDIX

A. Convergence of Distributed Collaborative VIO

Decentralized ADMM adopted by Alg. 1 was proven to have linear convergence performance on convex problems by Shi, Wei et. al. [45]. However, the bundle adjustment residual $r_{\mathcal{L}}(\hat{z}_{l_k}, \mathcal{X}_i)$ is not convex, and our algorithm introduces constraints on the manifold, which complicates the problem. Since RTR method compute a small step on tangent space $\mathfrak{se}(3)$ of the manifold, then retract back to the manifold $\mathbf{SE}(3)$, Update (8)-(11) are equivalent to iterating over $\mathfrak{se}(3)$ when the system is well initialized and initial pose are subtracted. We

consider this simplification update of Alg. 1:

$$\mathcal{X}_i^{t+1} = \arg \min_{\mathcal{X}_i} \left\{ r_{pb}(\mathcal{V}_i) + \sum_{k \in \mathcal{L}_i} \rho(\|r_{\mathcal{L}}(\hat{z}_{l_k}, \mathcal{V}_i)\|_{\Sigma_{\mathcal{L}}}) + h(\mathcal{V}_i) \right\} \quad (28)$$

$$h(\mathcal{V}_i) = \frac{1}{2} \sum_{v_j \in \mathcal{T}_i} \|\mathbf{v}_j^k - \mathbf{v}_j^t + (\tilde{\mathbf{v}}_j^k)^t\|_{\Sigma_{\rho_T}} + \rho_{\mathcal{L}} \sum_{l_i \in \mathcal{L}_i} \|l_i - l_i^t\| \quad (29)$$

$$\mathbf{v}_j^{t+1} = \frac{1}{n_i} \sum_{j=1}^{n_i} (\mathbf{v}_j^k)^{t+1}, \quad \forall \mathbf{v}_j \in \mathcal{V}_i \quad (29)$$

$$(\tilde{\mathbf{v}}_j^k)^{t+1} = (\tilde{\mathbf{v}}_j^k)^t + (\mathbf{v}_j^k)^t - \mathbf{v}_j^{t+1}, \quad \forall \mathbf{v}_j \in \mathcal{V}_i, \quad (30)$$

where \mathcal{V}_i is the set of all poses $\{\mathbf{v}_0 \dots\}$ on $\mathfrak{se}3$ in \mathcal{X}_i after subtraction of the initialized pose, $r_{pb}(\mathcal{V}_i)$ is the residual for prior and IMU factor. Because the rotation part of $\mathfrak{se}3$, i.e. $\mathfrak{so}3$ [46], and the angle-axis are equivalent, the parametrization of Eq. (28)-(30) is equivalent to [14].

According to [14], [71], we need to confirm that the gradient of each term in Problem (28) is local Lipschitz-continuous to confirm that the simplified update (8)-(11) can converge to a local minimum. In the Problem (28), the first term $r_{pb}(\mathcal{V}_i)$ is combination of several linear-least-square problems, which gradient are obviously local Lipschitz-continuous. Gradient of bundle adjustment residuals $r_{\mathcal{L}}(\hat{z}_{l_k}, \mathcal{V}_i)$ are shown to be Local Lipschitz-continuous when there is a minimum distance from the landmark to the camera, while Huber norm $\rho(\cdot)$ is equivalent to quadratic error in a small range and does not change its conclusion.

So similar to Theorem in [14], we confirm that the simplified update (8)-(11) can converge to a local minimum in a small range. So we argue that Alg. 1 can converge to a local optimum after a good initialization. For VIO, this degree of convergence is acceptable.

REFERENCES

- [1] H. Xu, Y. Zhang, B. Zhou, L. Wang, X. Yao, G. Meng, and S. Shen, “Omni-Swarm: A Decentralized Omnidirectional Visual-Inertial-UWB State Estimation System for Aerial Swarms,” *IEEE Trans. Robot. (TRO)*, 2022.
- [2] Y. Tian, Y. Chang, F. H. Arias, C. Nieto-Granda, J. P. How, and L. Carlone, “Kimera-multi: robust, distributed, dense metric-semantic slam for multi-robot systems,” *IEEE Transactions on Robotics*, 2022.
- [3] P.-Y. Lajoie, B. Ramtoula, Y. Chang, L. Carlone, and G. Beltrame, “DOOR-SLAM: Distributed, online, and outlier resilient slam for robotic teams,” *IEEE Robotics and Automation Letters*, vol. 5, no. 2, pp. 1656–1663, 2020.
- [4] S. Choudhary, L. Carlone, C. Nieto, J. Rogers, H. I. Christensen, and F. Dellaert, “Distributed mapping with privacy and communication constraints: Lightweight algorithms and object-based models,” *The International Journal of Robotics Research*, vol. 36, no. 12, pp. 1286–1311, 2017.
- [5] D. Saldana, B. Gabrich, G. Li, M. Yim, and V. Kumar, “Modquad: The flying modular structure that self-assembles in midair,” in *2018 IEEE International Conference on Robotics and Automation (ICRA)*. IEEE, 2018, pp. 691–698.
- [6] G. Loianno and V. Kumar, “Cooperative transportation using small quadrotors using monocular vision and inertial sensing,” *IEEE Robotics and Automation Letters*, vol. 3, no. 2, pp. 680–687, 2017.
- [7] X. Zhou, J. Zhu, H. Zhou, C. Xu, and F. Gao, “EGO-Swarm: A Fully Autonomous and Decentralized Quadrotor Swarm System in Cluttered Environments,” *arXiv preprint arXiv:2011.04183*, 2020.
- [8] P. C. Lusk, X. Cai, S. Wadhwania, A. Paris, K. Fathian, and J. P. How, “A Distributed Pipeline for Scalable, Deconflicted Formation Flying,” *IEEE Robotics and Automation Letters*, vol. 5, no. 4, pp. 5213–5220, 2020.
- [9] B. Zhou, H. Xu, and S. Shen, “Racer: Rapid collaborative exploration with a decentralized multi-uav system,” *arXiv preprint arXiv:2209.08533*, 2022.
- [10] H. Xu, L. Wang, Y. Zhang, K. Qiu, and S. Shen, “Decentralized visual-inertial-UWB fusion for relative state estimation of aerial swarm,” in *Proc. of the IEEE Intl. Conf. on Robot. and Autom. (ICRA)*. IEEE, 2020, pp. 8776–8782.
- [11] T. Qin, P. Li, and S. Shen, “Vins-mono: A robust and versatile monocular visual-inertial state estimator,” *IEEE Transactions on Robotics*, vol. 34, no. 4, pp. 1004–1020, 2018.
- [12] X. Zhou, X. Wen, Z. Wang, Y. Gao, H. Li, Q. Wang, T. Yang, H. Lu, Y. Cao, C. Xu *et al.*, “Swarm of micro flying robots in the wild,” *Science Robotics*, vol. 7, no. 66, p. eabm5954, 2022.
- [13] A. Eriksson, J. Bastian, T.-J. Chin, and M. Isaksson, “A consensus-based framework for distributed bundle adjustment,” in *Proceedings of the IEEE Conference on Computer Vision and Pattern Recognition*, 2016, pp. 1754–1762.
- [14] R. Zhang, S. Zhu, T. Fang, and L. Quan, “Distributed very large scale bundle adjustment by global camera consensus,” in *Proceedings of the IEEE International Conference on Computer Vision*, 2017, pp. 29–38.
- [15] D. Rosen, L. Carlone, A. Bandeira, and J. Leonard, “SE-Sync: A certifiably correct algorithm for synchronization over the special Euclidean group,” *Intl. J. of Robotics Research*, vol. 38, no. 2–3, pp. 95–125, Mar. 2019.
- [16] J. Briales and J. Gonzalez-Jimenez, “Cartan-sync: Fast and global se (d)-synchronization,” *IEEE Robotics and Automation Letters*, vol. 2, no. 4, pp. 2127–2134, 2017.
- [17] F. Dellaert, M. Kaess *et al.*, “Factor Graphs for Robot Perception,” *Foundations and Trends® in Robotics*, vol. 6, no. 1–2, pp. 1–139, 2017.
- [18] R. Mur-Artal, J. M. M. Montiel, and J. D. Tardos, “ORB-SLAM: a versatile and accurate monocular slam system,” *IEEE transactions on robotics*, vol. 31, no. 5, pp. 1147–1163, 2015.
- [19] V. Reijgwart, A. Millane, H. Oleynikova, R. Siegwart, C. Cadena, and J. Nieto, “Voxgraph: Globally consistent, volumetric mapping using signed distance function submaps,” *IEEE Robotics and Automation Letters*, 2020.
- [20] A. Cunningham, M. Paluri, and F. Dellaert, “DDF-SAM: Fully distributed SLAM using constrained factor graphs,” in *Proc. of the IEEE/RSJ Intl. Conf. on Intell. Robots and Syst.(IROS)*. IEEE, 2010, pp. 3025–3030.
- [21] A. Cunningham, V. Indelman, and F. Dellaert, “DDF-SAM 2.0: Consistent distributed smoothing and mapping,” in *Proc. of the IEEE Intl. Conf. on Robot. and Autom. (ICRA)*. IEEE, 2013, pp. 5220–5227.
- [22] N. Michael, S. Shen, K. Mohta, V. Kumar, K. Nagatani, Y. Okada, S. Kiribayashi, K. Otake, K. Yoshida, K. Ohno *et al.*, “Collaborative mapping of an earthquake damaged building via ground and aerial robots,” in *Field and Service Robotics*. Springer, 2014, pp. 33–47.
- [23] D. P. Bertsekas and J. N. Tsitsiklis, *Parallel and Distributed Computation: Numerical Methods*. Prentice-Hall, Inc., 1989.
- [24] Y. Tian, A. Koppel, A. S. Bedi, and J. P. How, “Asynchronous and parallel distributed pose graph optimization,” *IEEE Robotics and Automation Letters*, vol. 5, no. 4, pp. 5819–5826, 2020.
- [25] N. Boumal, “An introduction to optimization on smooth manifolds,” [Online]. Available: <http://www.nicolasboumal.net/book>
- [26] Y. Tian, K. Khosoussi, D. M. Rosen, and J. P. How, “Distributed certifiably correct pose-graph optimization,” *IEEE Trans. Robot. (TRO)*, 2021.
- [27] T. Qin, P. Li, and S. Shen, “Relocalization, global optimization and map merging for monocular visual-inertial slam,” in *2018 IEEE International Conference on Robotics and Automation (ICRA)*. IEEE, 2018, pp. 1197–1204.
- [28] K. Qiu, T. Liu, and S. Shen, “Model-based global localization for aerial robots using edge alignment,” *IEEE Robotics and Automation Letters*, vol. 2, no. 3, pp. 1256–1263, 2017.
- [29] A. I. Mourikis, S. I. Roumeliotis *et al.*, “A multi-state constraint kalman filter for vision-aided inertial navigation.” in *ICRA*, vol. 2. Citeseer, 2007, p. 6.
- [30] P. Zhu, P. Geneva, W. Ren, and G. Huang, “Distributed Visual-Inertial

Cooperative Localization,” *Proc. of the IEEE/RSJ Intl. Conf. on Intell. Robots and Syst.(IROS)*, 2021.

[31] P. Zhu, Y. Yang, W. Ren, and G. Huang, “Cooperative Visual-Inertial Odometry,” in *Proc. of the IEEE Intl. Conf. on Robot. and Autom. (ICRA)*, 2021.

[32] W. Gao and S. Shen, “Dual-fisheye omnidirectional stereo,” in *Proc. of the IEEE/RSJ Intl. Conf. on Intell. Robots and Syst.(IROS)*, 2017, pp. 6715–6722.

[33] C. Won, H. Seok, Z. Cui, M. Pollefeys, and J. Lim, “OmniSLAM: Omnidirectional localization and dense mapping for wide-baseline multi-camera systems,” in *2020 IEEE International Conference on Robotics and Automation (ICRA)*. IEEE, 2020, pp. 559–566.

[34] E. Plaut, E. Ben Yaacov, and B. El Shlomo, “3d object detection from a single fisheye image without a single fisheye training image,” in *Proceedings of the IEEE/CVF Conference on Computer Vision and Pattern Recognition*, 2021, pp. 3659–3667.

[35] P.-E. Sarlin, C. Cadena, R. Siegwart, and M. Dymczyk, “From coarse to fine: Robust hierarchical localization at large scale,” in *Proceedings of the IEEE Conference on Computer Vision and Pattern Recognition*, 2019, pp. 12716–12725.

[36] D. DeTone, T. Malisiewicz, and A. Rabinovich, “Superpoint: Self-supervised interest point detection and description,” in *Proceedings of the IEEE Conference on Computer Vision and Pattern Recognition Workshops*, 2018, pp. 224–236.

[37] R. Mur-Artal and J. D. Tardós, “ORB-SLAM2: an open-source SLAM system for monocular, stereo and RGB-D cameras,” *IEEE Transactions on Robotics*, vol. 33, no. 5, pp. 1255–1262, 2017.

[38] P. C. Ng and S. Henikoff, “Sift: Predicting amino acid changes that affect protein function,” *Nucleic acids research*, vol. 31, no. 13, pp. 3812–3814, 2003.

[39] J. Johnson, M. Douze, and H. Jégou, “Billion-scale similarity search with GPUs,” *IEEE Transactions on Big Data*, 2019.

[40] M. A. Fischler and R. C. Bolles, “Random sample consensus: a paradigm for model fitting with applications to image analysis and automated cartography,” *Communications of the ACM*, vol. 24, no. 6, pp. 381–395, 1981.

[41] L. Kneip, H. Li, and Y. Seo, “Upnp: An optimal $O(n)$ solution to the absolute pose problem with universal applicability,” in *European conference on computer vision*. Springer, 2014, pp. 127–142.

[42] L. Kneip and P. Furgale, “Opengv: A unified and generalized approach to real-time calibrated geometric vision,” in *2014 IEEE International Conference on Robotics and Automation (ICRA)*. IEEE, 2014, pp. 1–8.

[43] J. Civera, A. J. Davison, and J. M. Montiel, “Inverse depth parametrization for monocular slam,” *IEEE transactions on robotics*, vol. 24, no. 5, pp. 932–945, 2008.

[44] P. J. Huber, “Robust estimation of a location parameter,” in *Breakthroughs in Statistics*. Springer, 1992, pp. 492–518.

[45] W. Shi, Q. Ling, K. Yuan, G. Wu, and W. Yin, “On the linear convergence of the admm in decentralized consensus optimization,” *IEEE Transactions on Signal Processing*, vol. 62, no. 7, pp. 1750–1761, 2014.

[46] J. L. Blanco-Claraco, “A tutorial on $se(3)$ transformation parameterizations and on-manifold optimization,” *arXiv preprint arXiv:2103.15980*, 2021.

[47] F. L. Markley, Y. Cheng, J. L. Crassidis, and Y. Oshman, “Averaging quaternions,” *Journal of Guidance, Control, and Dynamics*, vol. 30, no. 4, pp. 1193–1197, 2007.

[48] S. Leutenegger, S. Lynen, M. Bosse, R. Siegwart, and P. Furgale, “Keyframe-based visual-inertial odometry using nonlinear optimization,” *The International Journal of Robotics Research*, vol. 34, no. 3, pp. 314–334, 2015.

[49] A. Rosinol, M. Abate, Y. Chang, and L. Carlone, “Kimera: an Open-Source Library for Real-Time Metric-Semantic Localization and Mapping,” in *2020 IEEE International Conference on Robotics and Automation (ICRA)*. IEEE, 2020, pp. 1689–1696.

[50] S. Agarwal, K. Mierle, and Others, “Ceres solver,” <http://ceres-solver.org>.

[51] K. Madsen, H. B. Nielsen, and O. Tingleff, “Methods for non-linear least squares problems,” 2004.

[52] Z. Peng, Y. Xu, M. Yan, and W. Yin, “Arock: an algorithmic framework for asynchronous parallel coordinate updates,” *SIAM Journal on Scientific Computing*, vol. 38, no. 5, pp. A2851–A2879, 2016.

[53] L. Carlone, R. Tron, K. Daniilidis, and F. Dellaert, “Initialization techniques for 3d slam: a survey on rotation estimation and its use in pose graph optimization,” in *2015 IEEE international conference on robotics and automation (ICRA)*. IEEE, 2015, pp. 4597–4604.

[54] R. Hartley, J. Trumpf, Y. Dai, and H. Li, “Rotation averaging,” *International journal of computer vision*, vol. 103, no. 3, pp. 267–305, 2013.

[55] D. Martinec and T. Pajdla, “Robust rotation and translation estimation in multiview reconstruction,” in *2007 IEEE Conference on Computer Vision and Pattern Recognition*. IEEE, 2007, pp. 1–8.

[56] J. Nocedal and S. J. Wright, *Numerical optimization*. Springer, 1999.

[57] J. Sola, “Quaternion kinematics for the error-state kalman filter,” *arXiv preprint arXiv:1711.02508*, 2017.

[58] J. J. Moré, “The levenberg-marquardt algorithm: implementation and theory,” in *Numerical analysis*. Springer, 1978, pp. 105–116.

[59] J. G. Mangelson, D. Dominic, R. M. Eustice, and R. Vasudevan, “Pairwise consistent measurement set maximization for robust multi-robot map merging,” in *2018 IEEE International Conference on Robotics and Automation (ICRA)*. IEEE, 2018, pp. 2916–2923.

[60] H. Yang, P. Antonante, V. Tzoumas, and L. Carlone, “Graduated non-convexity for robust spatial perception: From non-minimal solvers to global outlier rejection,” *IEEE Robotics and Automation Letters*, vol. 5, no. 2, pp. 1127–1134, 2020.

[61] G. Guennebaud, B. Jacob *et al.*, “Eigen v3,” <http://eigen.tuxfamily.org>, 2010.

[62] L. Meier, D. Honegger, and M. Pollefeys, “Px4: A node-based multithreaded open source robotics framework for deeply embedded platforms,” in *2015 IEEE international conference on robotics and automation (ICRA)*. IEEE, 2015, pp. 6235–6240.

[63] O. R. developers, “Onnx runtime,” <https://onnxruntime.ai/>, 2021, version: x.y.z.

[64] Y. Hu, T.-M. Li, L. Anderson, J. Ragan-Kelley, and F. Durand, “Taichi: a language for high-performance computation on spatially sparse data structures,” *ACM Transactions on Graphics (TOG)*, vol. 38, no. 6, pp. 1–16, 2019.

[65] K. M. Wurm, A. Hornung, M. Bennewitz, C. Stachniss, and W. Burgard, “Octomap: A probabilistic, flexible, and compact 3d map representation for robotic systems,” in *Proc. of the IEEE Intl. Conf. on Robot. and Autom. (ICRA)*, vol. 2, Anchorage, AK, US, May 2010.

[66] H. Oleynikova, Z. Taylor, M. Fehr, R. Siegwart, and J. Nieto, “Voxblox: Incremental 3d euclidean signed distance fields for on-board mav planning,” in *2017 IEEE/RSJ International Conference on Intelligent Robots and Systems (IROS)*. IEEE, 2017, pp. 1366–1373.

[67] V. Reijgwart, A. Millane, H. Oleynikova, R. Siegwart, C. Cadena, and J. Nieto, “Voxgraph: Globally consistent, volumetric mapping using signed distance function submaps,” *IEEE Robotics and Automation Letters*, vol. 5, no. 1, pp. 227–234, 2019.

[68] W. E. Lorensen and H. E. Cline, “Marching cubes: A high resolution 3d surface construction algorithm,” *ACM siggraph computer graphics*, vol. 21, no. 4, pp. 163–169, 1987.

[69] X. Chen, B. Zhou, J. Lin, Y. Zhang, F. Zhang, and S. Shen, “Fast 3d sparse topological skeleton graph generation for mobile robot global planning,” *arXiv preprint arXiv:2208.04248*, 2022.

[70] D. Schubert, T. Goll, N. Demmel, V. Usenko, J. Stückler, and D. Cremers, “The tum vi benchmark for evaluating visual-inertial odometry,” in *2018 IEEE/RSJ International Conference on Intelligent Robots and Systems (IROS)*. IEEE, 2018, pp. 1680–1687.

[71] S. Boyd, N. Parikh, E. Chu, B. Peleato, J. Eckstein *et al.*, “Distributed optimization and statistical learning via the alternating direction method of multipliers,” *Foundations and Trends® in Machine learning*, vol. 3, no. 1, pp. 1–122, 2011.